Integration of Transpiration Cooling and Shock Thrust Vectoring

by

Alexander Bukva

A thesis
presented to the University of Waterloo
in fulfillment of the
thesis requirement for the degree of
Master of Applied Science
in
Mechanical and Mechatronics Engineering

Waterloo, Ontario, Canada, 2022

Author's Declaration

This thesis consists of material all of which I authored or co-authored: see Statement of Contributions included in the thesis. This is a true copy of the thesis, including any required final revisions, as accepted by my examiners.

I understand that my thesis may be made electronically available to the public.

Statement of Contributions

Alexander Bukva was the sole author of Chapters 1, 2, and 6 which were written under the supervision of Jean-Pierre Hickey and were not written for publication. Additionally, Sections 3.1, 3.3, 4.2, 5.2 and 5.3 were authored solely by Alexander Bukva under the supervision of Jean-Pierre Hickey and were not written for publication.

The research presented in sections 3.2, 4.1 and 5.1 of this thesis consists in part of one paper written for publication and is an exception to sole authorship. Kevin Zhang, Nicholas Christopher and Jean-Pierre Hickey were co-authors of this work, with Alexander Bukva being the primary author. This research was conducted at the University of Waterloo by Alexander Bukva under the supervision of Jean-Pierre Hickey.

Citation:

A. Bukva, K. Zhang, N. Christopher, J.-P. Hickey, Assessment of turbulence modeling for massively-cooled turbulent boundary layer flows with transpiration cooling, Physics of Fluids 33 (2021) 095114

Abstract

Transpiration cooling is used for active thermal protection whereas shock thrust vectoring is an attitude control approach. Both concepts rely on the injection, at the wall, of a secondary fluid into a high-speed and high-temperature flow. The purpose of this work is to investigate, using theoretical and numerical methods, how both approaches could be integrated to simultaneously provide thermal protection and vector control to small-scale aerospace vehicles. This work has two parts.

Firstly, we assess Reynolds-averaged Navier-Stokes (RANS) turbulent closures for the prediction of a turbulent boundary layer with transpiration cooling via the comparison with a high-fidelity direct numerical simulation (DNS) database. This study considers the canonical zero-pressure gradient, flat-plate, turbulent boundary layer over a massively-cooled wall ($T_{wall} = \frac{1}{2}T_\infty$), with transpiration cooling. It is shown that the RANS-based turbulence models perform well in the qualitative estimation of the velocity and thermal boundary layer evolution at low-blowing ratios ($F = 0.2$ and 0.6%); more significant differences are noted at higher blowing ratios ($F = 2.0\%$). The RANS models, especially the Spalart-Allmaras model, over-predicts turbulence production near the wall, which results in faster growth in the boundary thickness; this error becomes more pronounced at higher blowing ratios. Despite the greater mixing of momentum, the thermal mixing is under-predicted compared to the DNS in the uniform blowing case but over-predicted for the slit case. These results suggest that modeling errors in the temperature distribution due to the turbulent thermal flux modeling can be significant even if the velocity is correctly modeled.

The second part of the work investigates the integration of transpiration cooling and shock vector control (SVC). After validation against experimental data, the blowing ratio, inlet Mach number, entrance length and turbulence were varied to understand the functional relationship between these variables. The Mach line profile, which delineates the sub- from supersonic region of the flow, is a critical feature that has a direct impact on the resultant shock wave formation. The RANS model was compared to the analytical blunt body dynamic model to estimate separation distance and good agreement was found. From this

result it was concluded the transpiration cooling and SVC could be reasonably integrated for single stage rockets.

Acknowledgements

Firstly, I would like to thank Dr. Jean-Pierre Hickey, my MASc supervisor, for his guidance in my work. He has been a great mentor to me in the world of fluid mechanics and high performance computing. I thank him especially for allowing me to learn on my own - this is the greatest skill I have learned, and I will treasure this for the rest of my life.

I would also like to thank Syed Imthiaz Ahamed Syed Abid Hussain for our academic discussions in both undergrad and grad school. You taught me so much about high speed flows and it was a pleasure to learn from you.

Lastly, I would like to thank my family and loved ones for providing me their unwavering love and support.

Dedication

This work is dedicated to my family, for all their love and support.

Table of Contents

List of Figures

List of Tables

Nomenclature

Characters

Symbol	Description	Unit
k	turbulent kinetic energy	
ω	specific dissipation of turbulent kinetic energy	
ϵ	rate of dissipation of turbulent kinetic energy	
h	penetration height	m
ρ	density	$\mathrm{kg} \cdot \mathrm{m}^{-3}$
$\boldsymbol{u}$	velocity vector	$\mathrm{m} \cdot \mathrm{s}^{-1}$
t	time	s
x	position vector	m
p	pressure	$\mathrm{kg} \cdot \mathrm{m}^{-1} \cdot \mathrm{s}^{-2}$
$\boldsymbol{\delta_{ij}}$	Kronecker tensor	1
$\boldsymbol{\sigma}$	viscous stress tensor	$\mathrm{kg} \cdot \mathrm{m}^{-1} \cdot \mathrm{s}^{-2}$
e	specific total energy	$\mathrm{m}^2 \cdot \mathrm{s}^{-2}$
q	heat flux vector	$\mathrm{m}^2 \cdot \mathrm{s}^{-2}$
ψ	compressibility	K
R	specific gas constant	$\mathrm{m}^2 \cdot \mathrm{s}^{-2} \cdot \mathrm{K}^{-1}$
T	temperature	K
μ	dynamic viscosity	$\mathrm{kg} \cdot \mathrm{m}^{-1} \cdot \mathrm{s}^{-1}$

a	speed of sound	$\mathrm{m} \cdot \mathrm{s}^{-1}$
M	Mach number	1
Ω	magnitude of vorticity	
ν	kinematic viscosity	$\mathrm{m}^2 \cdot \mathrm{s}^{-1}$
c_p	specific heat capacity at constant pressure	$\mathrm{m}^2 \cdot \mathrm{s}^{-2} \cdot \mathrm{K}^{-1}$
ν_t	turbulent viscosity	$\mathrm{m}^2 \cdot \mathrm{s}^{-1}$
δ_i	non-dimensional boundary layer height	1
δ_{99}	dimensional boundary layer height	1
F	Blowing ratio	1
$\boldsymbol{V_w}$	Darcy velocity	$\mathrm{m} \cdot \mathrm{s}^{-1}$
Re	Reynolds number	1
Re_τ	Shear stress Reynolds number	1
Re_θ	momentum thickness Reynolds number	1
y^+	non-dimensional wall normal distance	1
u^+	non-dimensional x-velocity	1
L	Domain length	m
H	shape factor	1
δ_2	displacement thickness	m
θ	momentum thickness	m
Pr_t	turbulent Prandtl number	1
γ	ratio of specific heat	1

Subscripts

Symbol	Description
i, j, k	Einstein subscripts

x, y, z	unit vector directions
t	turbulent quantity
∞	freestream values
0	stagnation properties
s	location of separation shock
m	start of injection
w	wall
FTT	flow through time

Operators

Symbol	Description
O	order of magnitude
Δ	difference
∇	gradient operator
$\nabla\cdot$	divergence operator
∇^2	Laplace operator

Abbreviations

Acronym	Description
RANS	Reynolds-averaged Navier–Stokes
SVC	shock vector control

Chapter 1

Introduction

Advanced thermal protection systems (TPS) are at the cornerstone of modern space transportation development. The ability to limit extreme thermal loads on combustion chamber walls, the exterior body during re-entry, or during hypersonic flight is central to many of the emerging paradigms of "new space"; re-usability, increased safety and efficiency. More practically, continual improvements to TPS can lead to increased performance (e.g. through higher combustion chamber temperatures), an overall weight reduction and a reduction of manufacturing costs via the use of lower-cost materials.

A variety of physical mechanisms can be used to reduce the thermal loading for space applications, such as: ablative materials [14], film cooling [15], or passive transitional flow control-based surface properties [16] to name a few. Some of the recent advances in TPS have been summarized by Zhu et al. [17]. Another promising active TPS is transpiration cooling (see Figure 1.1). This method of cooling has been recently considered for chamber walls [18] and airframe cooling on re-entry [19, 20] by major aerospace organizations. Transpiration cooling involves injecting coolant through the porous and permeable side walls into a hot boundary layer flow. This effectively cools the walls by convective cooling within the porous material and accumulation of a coolant film on the inside face of the boundary layer wall, similar to film cooling. The cooling effectiveness of transpiration cooling is superior to that of film cooling, and for this reason has renewed interest by

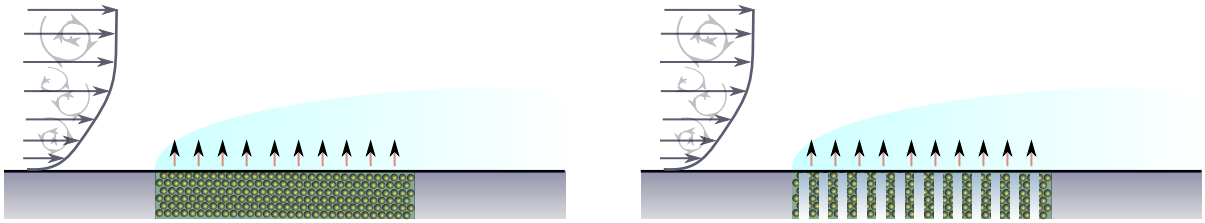

Figure 1.1 Illustration of transpiration cooling with uniform blowing (left) and slit/inhomogeneous blowing (right) from [1].

researchers. With the coming of age of modern metal additive manufacturing, especially with architected lattice structures such as triply periodic minimal surfaces, porous metal walls can be seamlessly integrated into structural metallic parts. By effectively cooling the side walls, engineers can resort to more inexpensive materials that enable the use of these modern additive manufacturing techniques.

Although there are advantages to using transpiration cooling, there are also a few disadvantages. For rocket engines, fuel injected as coolant will not contribute as efficiently to the impulse [18]. Therefore, it is imperative to design the system to use as little coolant as possible. Additionally, the use of transpiration cooling involves diverting propellant or transporting dedicated fluid towards the side wall for cooling. The transpiration cooling system alos includes additional pumps and valves as seen in Figure 1.2. The increased complexity and weight of the active thermal protection system often negatively impacts the cost/benefit analysis in many applications. Therefore, creating a dual-use for the transpiration cooling architecture is highly desired.

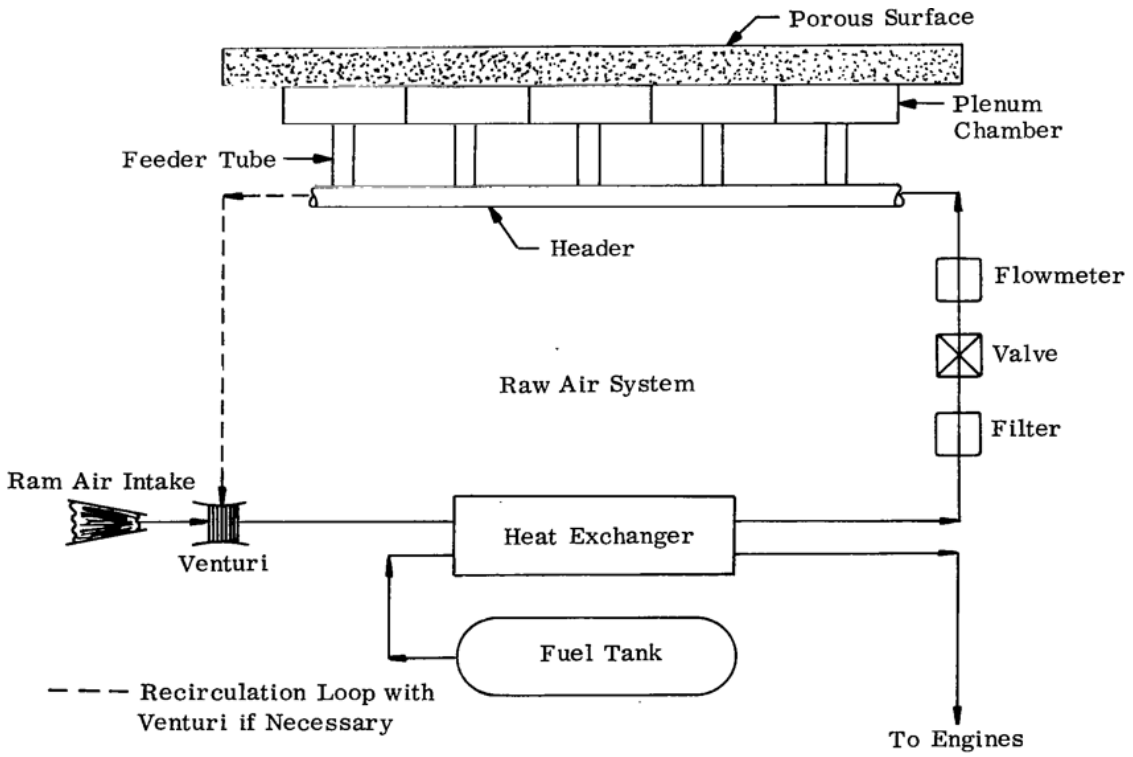

Figure 1.2 Typical transpiration cooling set-up taken from McConarty and Anthony [2]

1.1 Integrating transpiration cooling and shock vector control

This work explores, via numerical simulations, the novel use of transpiration cooling for thrust vectoring applications. A dual-use of transpiration cooling can be achieved by combining the fluidic injection with shock thrust vectoring in high-speed flow applications. In reaction engines, the propellants react and expand in the combustion chamber. A converging-diverging nozzle is used to accelerate the flow above the speed of sound and, in doing so, thrust is created. The primary function of propulsion systems is to provide a propulsive force to aeronautical or astronautical vehicles during flight. Dual functionality of transpiration cooling architectures can be achieved if the vector (magnitude and direction) of the trust can be controlled. For single engine vehicles, there are 4 main thrust vectoring methods[21]:

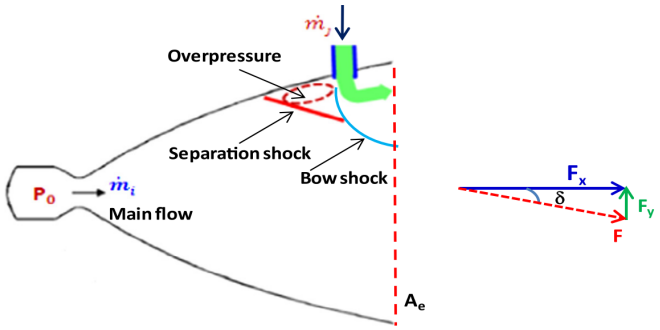

Figure 1.3 Example of a typical SVC system, taken form Sellam et al. [3]

1. Mechanical deflection of the nozzle or thrust chamber.

2. Insertion of heat-resistant movable bodies onto the exhaust jet. These experience aerodynamic forces and cause a deflection of part of the exhaust gas flow.

3. Separate thrust-producing devices that are not part of the main flow through the nozzle.

4. Injection of fluid into the side of the diverging nozzle section, causing an asymmetrical distortion of the supersonic exhaust flow due to shock wave formation.

Item number 4 is commonly referred to as a shock-vector control (SVC) system. Its flow characteristics can easily be integrated with transpiration cooling, making it an ideal candidate to study. An overview of a typical shock-vector control (SVC) system is shown in Figure 1.3.

1.2 Contribution and organization of thesis

This work explores the potential dual-use of transpiration cooling and shock thrust vectoring for high-speed flow applications. Ideas along this line of thought have been proposed by Billig [22], but proof commercial viability, technical feasibility and an extensive evaluation of these ideas have yet to take place. This work uses a systematic approach to first understand the accuracy of the turbulence modeling assumptions in these complex flows before

conducting detailed numerical investigations into the shock thrust vectoring potential. This numerical work serves as the basis for validating a low-order model of this technology.

The contributions of this work are:

- Evaluation of turbulence modelling and error quantification for transpiration cooling (Chapter 5.1 and published papers: Bukva et al., AIAA Hypersonics and Space Planes 2020 [23] and Bukva et al., Physics of Fluids, 2021 [24])
- Validation of oblique shock generation with transpiration cooling at high-Mach number flows (Chapter 5.2) and quantification of pressure rise in the post-shock region. (paper in preparation)
- Development of a low-order model to predict the thrust vectoring potential for transpiration cooling applications. (paper in preparation)

These contributions highlight the potential dual-use application of transpiration cooling and shock thrust vectoring for space applications.

The thesis is organized as follows: Chapter 2 covers the literature review on both transpiration cooling and shock thrust vector control. Next, in Chapter 3, the computational details of the numerical solver are discussed. In Chapter 4, validation using experimental data is provided. The primary results on the transpiration cooling focuses on modeling the heat flux and turbulence compared to a DNS(Direct Numerical Simulation) database. The SVC(Shock Vector Control) simulations validated against experimental results in which the wall temperature, pressure distributions and shock wave compositions is compared. Finally, Chapter 5 expands on the results of the aforementioned simulations and propose a low-order modeling strategy.

The chapters in this thesis are split into two distinct parts. The first part addresses transpiration cooling at low Mach numbers, while the second focuses on a combination of high-speed transpiration cooling and SVC. As turbulence plays a dominant role in SVC application, it was paramount to adequately validate the turbulence modeling assumptions

in transpiration cooling. This presents a very challenging setup for standard Reynolds-Averaged Navier-Stokes (RANS) approaches. The dearth of near-wall experimental data for turbulent transpiration cooling made the assessments difficult to undertake. Therefore, a DNS database was used as a point of comparison for the RANS simulations. This further allowed for a great deal of refinement in the model, as the whole flow field was resolved. This fundamental investigation resulted in a conference proceeding [23] and a publication [24]. With this new found understanding of the turbulence modeling uncertainty, the study continued to a high-speed flow regime which focused on the use of transpiration cooling for SVC applications. The numerical setup for each part is detailed in this work.

Chapter 2

Literature Review

The literature review aims to inform the reader on the work done in the areas of transpiration cooling and shock-vector control. The literature review focuses on each area, namely transpiration cooling and shock thrust vector control (SVC), separately and then discuss the small but meaningful work done when both aspects are combined.

2.1 Transpiration Cooling

Since the integration and optimization of transpiration cooling systems can be very challenging and costly, numerical tools are critical in determining the heat fluxes and resulting wall temperatures. However, modeling the physical phenomena in transpiration cooling is inherently difficult, as there are multiple mass and heat transfer mechanisms occurring simultaneously over a wide range of spatio-temporal scales. Within the porous wall, conduction and convection from the fluid cools the solid; furthermore, the liquid-to-gas phase change (in the case of a liquid coolant) can absorb a substantial amount of thermal energy– thus greatly increasing wall cooling. As the coolant is effused from the porous media into the turbulent boundary layer, the cooler fluid offers a thermal buffer to protect the wall from the hot gas, reducing the heat transfer into the wall. Therefore, a comprehensive simulation tool must not only model the porous material, but also must model the reduction of heat

transfer into the porous material via the film accumulation effect. These effects are heavily modulated by the turbulence in the boundary layer and properties of the injected fluid [25].

Recently, advances in computational efficiency have allowed researchers to perform direct numerical simulation (DNS) studies of transpiration cooling [26, 27]. DNS is a valuable tool for supplementing experimental data, as it enables the full resolution of all turbulent scales and provides information about the physics of the problem. The severe computational cost of DNS studies often makes the approach non-viable for realistic engineering applications. Nonetheless, the use of DNS can provide valuable understanding of transpiration cooling that can be used to improve the lower-order turbulence modeling strategies in large-eddy simulation (LES) or Reynolds-averaged Navier-Stokes (RANS) solvers. Although experimental results are critical, they remain rare [28–32] and are plagued with the same near-wall measurement uncertainty and challenges of classical wall-bounded turbulent flows.

In spite of the need to better understand the modulating effect of transpiration cooling on boundary layer turbulence, only a limited number of DNS studies on transpiration cooling are found in the open literature. Avsarkisov et al. [33] performed DNS of wall transpiration in a periodic turbulent Poiseuille flow in order to validate a logarithmic wall scaling law. As a followup work, Kraheberger et al. [34] computed transpiration in a periodic turbulent Couette flow, and investigated the near wall turbulent structures. In both simulations, the flow domain was streamwise and spanwise periodic, with one blowing wall and one suction wall in order to obtain a mass-balanced, statistically-steady turbulent flow; this canonical setup provides a more theoretical focus on transpiration cooling. Cerminara et al. [26, 35] performed a DNS in which transpiration coolant is injected into a laminar boundary layer, which transitions to turbulence downstream of the injection point. The same group has additionally investigated coolant flow through individual spherical pores and subsequent injection into a laminar boundary layer [36]. Recently, a first DNS of a spatially-evolving fully turbulent boundary layer with transpiration cooling was presented by Christopher et al. [27, 37]. These simulations were used to better understand the film accumulation effects and the overall cooling efficiency through transpiration injection at the wall. These simulations

were also used to address wall modeling considerations with transpiration cooling [23].

Although DNS provides valuable insight, the excessive computational cost means that, for engineering design, simplifying assumptions need to be made in order to model the effect of the turbulence on the mean flow. Reynolds-averaged Navier-Stokes(RANS) equations, which model the effects of turbulence via an additional eddy viscosity term, represent the primary modeling approach used for the predictive aerothermal design. Recent works [38] have compared experimental results to RANS-based simulations, showing good predictive capabilities. Accurate near-wall turbulence modeling is predicated on modeling the concurrent physical effects occurring due to wall blowing, and compounded by the variable viscosity and density of the injected flow. There are many proposed modifications to the RANS model to account for these effects. To better capture the correct heat transfer effects, they remain mostly *ad hoc* modifications based on increasing the near-wall dissipation properties, that have only been validated at low blowing ratios.

Menter developed one of the most robust general turbulence models, the k-ω SST model, which is a combination of the k-ω model for the inner parts of the boundary layer and the k-ϵ model in the freestream [39]. Menter's model led Wilcox to develop a correction for the dissipation, ω, under transpiration conditions in the two-equation model [40]. This correction was designed to match the experiments done by Andersen et al. [41]. In a similar endeavour, Chedevergne et al. [29] developed a correction for the k-ω SST model that is only dependent on the blowing ratio and did not affect results for non-transpiration boundary layers. Chedevergne et al. compared their results to the Wilcox correction and CS model, showing better performance in modeling the velocity profile and friction coefficient in most cases. Hink et al. [28] extended the variable density, one equation Spalart-Allmaras (SA) model to account for wall effusion. The extension of the model is based on a modification of the characteristic wall distance d, and uses Wilcox' blowing parameter S_B, to estimate the effective effusion wall distance. This results in a change to the specific dissipation at the wall which accounts for the effects of wall blowing. Bellettre et al. [42] showed promising results using the RNG k-ϵ model, in which the effects of blowing on turbulence modeling have a slightly more physical basis. However, to the

authors' knowledge, this model has never been compared to any of the previous models mentioned. A similar approach was taken by Munk, using a seven-equation Reynolds stress model, which was more accurate than the Wilcox correction for the k-ω SST model [43]. Prokein et al. [44] took a different approach by showing that transpiration can be physically modeled in OpenFoam by controlling the inlet boundary conditions, and did not use any model corrections in their simulations. These models have been assessed and tested against experimental data, although the validation has been limited to low blowing ratios. Standard RANS turbulence models have also been shown to provide good predictive estimates in non-adiabatic, turbulent flow conditions [45, 46].

2.2 Developments in Shock Vector Control

Shock thrust vector control relies on fluidic injection into a supersonic nozzle to generate a shock wave. A differential pressure distribution on a portion of the side wall of an axisymmetric nozzle creates mechanical force that can modify the thrust of a rocket. SVC is a well established field of research. It has been researched analytically, numerically and experimentally.

Early research on SVC was focused on developing analytical models to predict the overall behaviour of the system. Four main analytical theories have been formulated for SVC: blunt-body dynamics, blast-wave theory, linear analysis and boundary layer separation. The Blunt-body dynamics model was developed in 1964 by Zukoski and Spaid[4] and Spaid[47], a schematic is shown in Figure 2.1. This model assumes (1) the jet is sonic, (2) that no mixing occurs between the primary and injected flow, (3) the interface between the injectant and primary flow is a quarter sphere followed by an axisymmetric half cylinder, (4) the interface between separated flow downstream of the injector and the injectant always lies inside the half cylinder mentioned in (3). This model used the penetration height, h, of the blunt model and relates it to the separation distance of the shock; In 1967, Zukoski [48] correlated h to the separation distance in 2D using a proportionality constant for both laminar and turbulent flows. Maarouf [12] correlated h to the separation distance

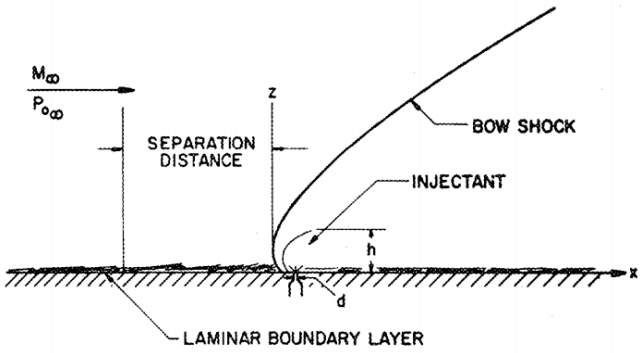

Figure 2.1 Blunt body schematic, taken from Zukoski and Spaid [4]

geometrically using a tangent constraint placed on the separation shock and the edge of the blunt body for 3D flows. The blunt body model was validated in many published works [3, 7, 49, 50], but the main criticism of the model is the need for correction factors to match analytical and experimental results [51].

Secondly, the blast-wave theory was first applied to SVC by Broadwell [52]. The blast-wave theory is based on the idea that the injected fluid acts as a source of mass, momentum and energy in the primary stream and the effects of the source are independent of the wall boundary layer. The modelled flow source is concentrated at a point and can either be a gas or fluid that vaporizes. In addition to handling phase change, blast-wave theory can account for chemical reactions through changes in the energy source term. Some of the drawbacks of the model are: poor predictions of the upstream pressure, no consideration of shock wave interactions and no resolution of the injection parameters, such as injector diameter and position.

Thirdly, linear analyses was employed by Walker and Shandor [5] to model SVC. The problem is idealized as a constant area mixing between the injectant and supersonic flow; the model is shown schematically shown in Figure 2.2. The ability to predict specific impulse was validated for small mass flow rates. At larger mass flow rates, this model breaks down and offers no predictive value for specific impulse. It also cannot predict the results of the resulting shock wave angle and separation distance.

Finally, the boundary layer separation model was formulated by Wu et al. [53] using an

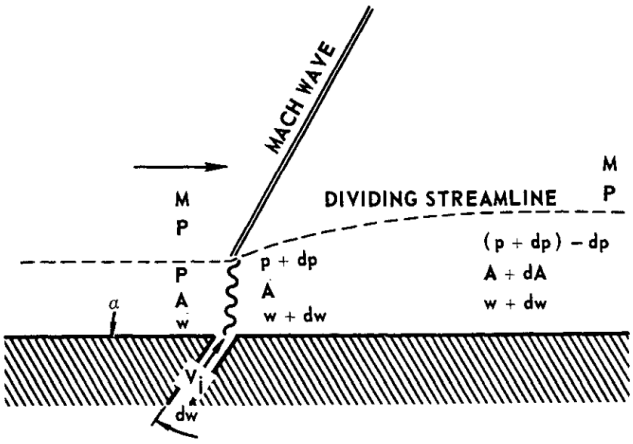

Figure 2.2 Linear analyses schematic, taken from Walker and Shandor [5]

eight equation model and the geometry of a 2D flow. The boundary layer separation model accounts for the separation preceding the injector port. It does not scale well into 3D due to complex geometric constraints[11].

Each of the aforementioned analytical models has faced criticism for their ability to accurately predict the thrust vectoring in real world systems. To further emphasize the overall lack of complete predictability of the previously mentioned analytical models, the reader is directed to Figure 2.3. The complex physics present in the horseshoe vortex, the complex bow shock, the trailing injector wake vortices and the jet plume crossflow vortices make an all encompassing analytical model unlikely to be derived or effectively implemented. These models have their place in approximating injector performance and directing initial designs, but experimental and numerical investigation must be conducted to fully understand performance. Younes and Hickey [11] have conducted an investigation and found that of the 4 analytical models presented, the blunt-body model provides the best predictive ability for forces and deflection angle for a small Bell shaped nozzle.

Aside from the analytical SVC models, many experimental works have been conducted to characterize overall SVC performance. Wing and Giuliano [54] showed that overexpanded supersonic nozzles were able to be thrust vectored up to 18°. They also showed that, at design conditions, the thrust could be vectored 13° without significant power losses in

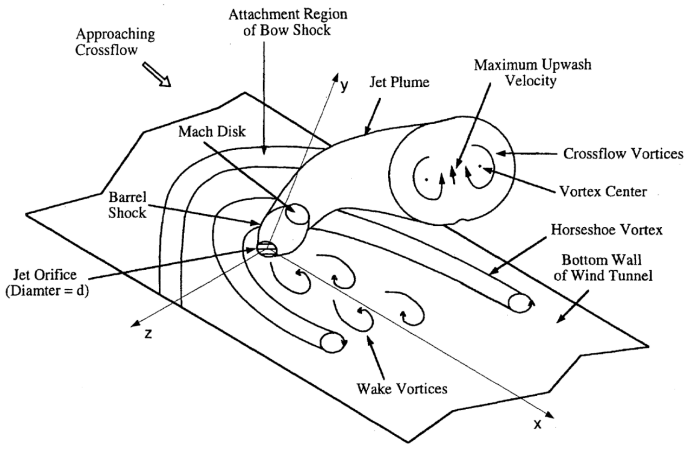

Figure 2.3 Schematic of the flowfield of a transverse jet injected into a supersonic flow, taken from Santiago and Dutton [6]

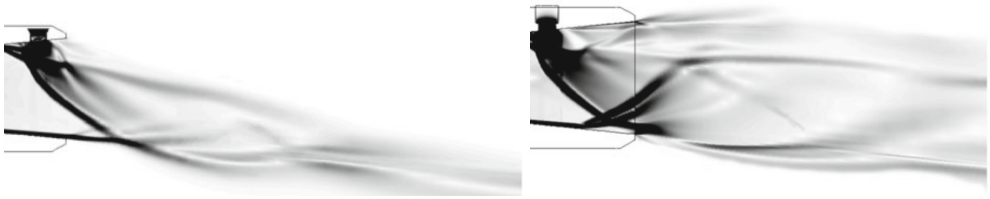

Figure 2.4 Numerical generated Schlieren images of Injection Port (left) closer to nozzle exit, (right) closer to nozzle throat, taken from Zmijanovic et al. [7]

thrust efficiency. It was shown experimentally and numerically by Anderson et al. [55] and Waithe and Deere [56], that multiple injection ports increase the thrust performance at nozzle pressure ratios of 4 or lower. The adverse effect of an impinging shock on the opposite wall section of the injector was shown by many [7, 55, 57]. This was caused by placing the injector too far into the diverging section of the nozzle; an example of experimental results can be seen in Figure 2.4. Considerable work was also done to identify the effect of different gas injectants. For example, Sellam et al. [3] found when the product of molecular mass and specific heat ratio is larger for the secondary gas, higher vectored angles can be achieved. Additionally, certain gases like helium, can produce the same deflection with lower mass flow rate. However, the performance of the thrust is inversely impacted by product of molecular mass and specific heat ratio. Similar results were found

numerically by Deng et al. [57].

The effect of turbulence plays a predominant role in the physics of SVC affecting the separation distance, post-shock turbulence intensity, and overall shock structure. To study this problem numerically, careful attention needs to be placed on the turbulence models, in some cases the turbulence models need to be modified to account for the physical particularities of SVC. For turbulent flows, a simple 2-equation model can be used but irregularities occur at solid surfaces with shock-induced separated flow, so a damping function or wall model are needed [7, 56, 58]. Otherwise, a certain error in the simulation must be accepted as done by Deng et al. [57], and simulations can serve a more parametric function.

2.3 Combining Transpiration cooling and SVC

Combining transpiration cooling and SVC is a difficult task, as it stacks the previously mentioned complexities of both problems into a new and more difficult obstacle. Research papers in this specific topic are rare and hard to replicate in a purely numerical manner without the aid of experiments, as is the case for this thesis.

A few noteworthy studies include the numerical and experimental investigation by Jiang et al. [59], where a shock generator was placed in front of a porous plate. The results show that the transpiration cooling efficiency is reduced because of the impinging shock wave, which decreases the fluid velocity near the porous wall, increasing static temperature. From a modelling perspective, the basic continuity, momentum and energy equations were used with the $k - \epsilon$ model to model turbulence. In this study, the authors paid much attention to modelling the coolant tank and porous material, using the Brinkman–Forchheimer extended the Darcy model to estimate velocity and local thermal equilibrium to approximate temperature. From a validation perspective, there was only a comparison between the angle of the reflecting shock wave between walls. Experimental near wall measurements are not easy to obtain for this type of experiment to compare to numerical results. A similar experimental study was done by Holden [60]. Both studies were focused on the decrease in cooling

efficiency caused by an incoming shock rather than any SVC considerations, although those questions could have been explored. Gülhan and Braun [9] conducted a study of supersonic flow over a porous flat plate, using infrared cameras to measure the surface temperature of the plate for both laminar and turbulent freestream flows. To the author's best knowledge, there have not been any studies focusing on the SVC characteristics of supersonic transpiration flow. Furthermore, a parametric study for the combination of transpiration cooling and SVC has not been complete and published. However, a patent published by Billig [22], seems to combine transpiration cooling and SVC into one system, but using a different method than described previously. Instead of using the transpired fluid as a means of SVC, the patent combines both concepts separately. There is steam generated in the system below the combustion chamber walls that can be conveyed to the transpiration region to cool the walls of the combustion chamber; but can also be diverted to multiple conventional SVC injectors to control the flight path. Similar to the rest of the combined transpiration and SVC systems, detailed information was not available. The use of the system could not be found in a real world example and the schematics that were available online were of bad quality and were not legible.

Chapter 3

Computational details

In this chapter, the computational details of the simulations are discussed. The present chapter is divided into three sections. First, the characteristics of the Reynolds Averaged Navier-Stokes (RANS) solver, namely OpenFoam, are discussed. The discussion focuses specifically on the details that are common to all simulations in the thesis, including the numerical schemes implemented into the solver. Section 3.2 examines the details of the compressible transpiration cooling simulations. Subsection 3.2.1 defines the parameters of the DNS database, while subsection 3.2.2 similarly defines the RANS model that is subsequently compared to the DNS database. These subsections define the sum of the compressible transpiration cooling setup, and alert the reader to minor differences in boundary conditions, turbulent resolution and grid size to be kept in mind during validation and comparison of results. Finally, section 3.3 details the parameters of a simulated laminar hypersonic flow, injected with a transpired fluid to achieve shock vector control. Subsection 3.3.1 details the experimental case on which the simulation was designed and the simulated domain and boundary conditions. Subsection 3.3.2 details additional changes made to the original case to explore the parameters of SVC. Upon completion of this chapter the reader will be made aware of two distinct sets of simulations, a low Mach number, turbulent, compressible flow and hypersonic transpiration case with SVC, and the associated details and set-up of two distinct set of simulations.

3.1 Solver specific computational details

The software used for all simulated cases was `OpenFOAM-v2012`, which is an updated version of the solver described by Weller et al. [61]. It was chosen because it is robust, accurate and can be easily run using parallel computing on the Compute Canada architecture. Specifically, the `rhoCentralFoam` solver was used, which is a segregated, compressible, density-based, transient solver. The governing compressible Navier-Stokes equations,in conservative form, are presented below using Einstein notation:

$$\frac{\partial \rho}{\partial t} + \frac{\partial (\rho u_j)}{\partial x_j} = 0 \tag{3.1}$$

$$\frac{\partial (\rho u_i)}{\partial t} + \frac{\partial (\rho u_i u_j + p\delta_{ij})}{\partial x_j} = \frac{\partial \sigma_{ij}}{\partial x_j} \tag{3.2}$$

$$\frac{\partial (\rho e)}{\partial t} + \frac{\partial [(\rho e + p)u_j]}{\partial x_j} = -\frac{\partial q_j}{\partial x_j} + \frac{\partial (\sigma_{ij} u_i)}{\partial x_j} \tag{3.3}$$

In the above equations, e is the total energy (sum of internal and kinetic energy), σ_{ij} is the viscous stress tensor, and q_j is the heat flux vector. The `rhoCentralFoam` algorithm is described by Nielsen [62] as follows:

1. Solve for density using the continuity equation
2. Solve for velocity using the momentum equation
3. Solve for temperature using the energy equation
4. Solve for pressure using the equation of state

The thermophysical properties are evaluated using the `psiThermo` module. The compressibility, defined as $\psi = \frac{\partial \rho}{\partial p}$, is calculated using the gas constant R and the temperature at each cell as given by equation (3.4).

$$\psi = \frac{1}{RT} \tag{3.4}$$

The dynamic viscosity, μ, is assumed to follow Sutherland's law. As temperature changes throughout the flow, so will μ following equation (3.5).

$$\mu = \frac{A_s\sqrt{T}}{1 + \frac{T_s}{T}} \tag{3.5}$$

For a standard dimensional cases $A_s = 0.000001458$, and $T_s = 110.4$ K[63, 64]. The specific heat at constant pressure, c_p, is assumed to be constant. We take c_p to be $1006\frac{J}{kgK}$ [65]. An ideal gas is assumed using the module `perfectGas` to model the equation of state. `PerfectGas` uses the ideal gas law to calculate the density at each cell, given by equation (3.6).

$$\rho = \psi p \tag{3.6}$$

The `OpenFOAM` solver allows the user to choose between internal energy and enthalpy as the form of energy used in the conservation equation. For these simulations internal energy was selected by using the `sensibleInternalEnergy` module. The molecular weight of air used in the simulations is $28.97\frac{kg}{kmol}$ by adding the weight of each component of air[65].

The numerical schemes used in `rhoCentralFoam` are not rigid but can be altered by the user. The time derivatives, $\frac{\partial}{\partial t}$, are approximated using backward Euler, which is a first-order implicit scheme given, in general form, by:

$$u_{k+1} = u_k + \Delta t \frac{du}{dt}(t_{k+1}, u_{k+1}) \tag{3.7}$$

Accuracy in time is not of principal concern as the simulation is run to a steady state, so quick computation time was weighted more favourably than a more accurate temporal resolution. The module used to approximate the gradient (∇), divergence ($\nabla\cdot$) and Laplacian (∇^2) terms are `Gauss linear`. The Gauss schemes indicates that standard finite volume method is used, where Gaussian integration occurs between cell faces. The name linear indicates that the face values are interpolated by a central difference method between adjacent cell centers making all spatial terms second-order accurate. The general second-order scheme for gradient and divergence terms can be seen in equation (3.8), where h is the distance between sampled points.

$$\frac{du}{dx}(x_i) = \frac{u(x_{i+1}) - u(x_{i-1})}{h} \tag{3.8}$$

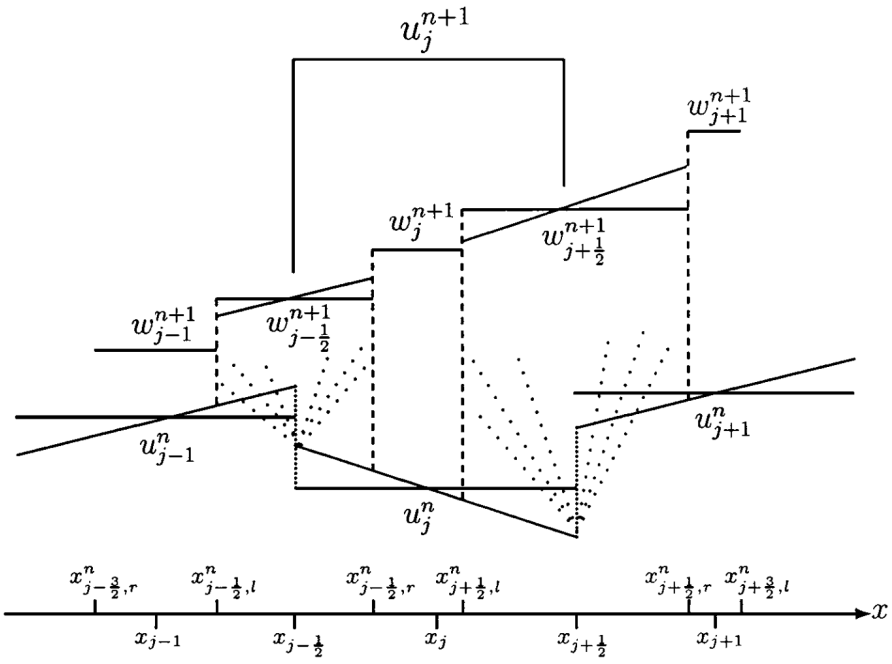

Figure 3.1 Schematic of the Kurganov and Tadmor [8] central scheme

The general second-order scheme for Laplacian terms can be seen in equation (3.9):

$$\frac{d^2u}{dx^2}(x_i) = \frac{u(x_{i+1}) - 2u(x_i) + u(x_{i-1})}{h^2} \tag{3.9}$$

On top of the regular OpenFOAM schemes used to run simulations, the Kurganov and Tadmor (KT) central scheme is used to further refine the face fluxes[8]. This scheme is in the MUSCL (Monotonic Upstream-centered Scheme for Conservation Laws) group of solvers and is TVD (total variation diminishing), allowing high-resolution solution of discontinuities. The KT scheme uses more precise information about the local speed of wave propagation in order to average over the non-smooth parts of the solution. The KT procedure can be seen in pictorial form in Figure 3.1. The procedure starts by calculating the local speed of propagation at the cell boundary $x_{j+\frac{1}{2}}$. Due to the finite propagation speed, the points $x^n_{j-\frac{1}{2},l} = x_{j-\frac{1}{2}} - a^n_{j+\frac{1}{2}}\Delta t$ and $x^n_{j+\frac{1}{2},r} = x_{j+\frac{1}{2}} + a^n_{j+\frac{1}{2}}\Delta t$ separate smooth and non-smooth regions. This procedure essentially traps the non-smooth parts of the solution domain into a smaller control volume of $2a^n_{j+\frac{1}{2}}\Delta t$. The greater number of smaller control volumes now approximate the domain, as represented by dashed vertical lines in Figure

3.1. The last step involves converting the oversampled grid, w, back into the original grid to get the value of u_j^{n+1}. The mathematical procedure needed to implement this scheme is presented in Kurganov and Tadmor [8], interested readers are referred to the original paper.

For cases in the turbulent regime, additional transport equations must be solved to compute the turbulent viscosity of the flow. Two different turbulence models are used in this work, the $k-\omega$ SST and the SA model. The selection of the model for a given case will be discussed in later sections. The $k-\omega$ SST model was developed by Menter [39] and combines the k-ω model for the inner parts of the boundary layer and the k-ϵ model away from the wall. The $k-\omega$ SST model calculates turbulent viscosity as shown in equation 3.10.

$$\mu_t = \frac{\rho a_1 k}{max(a_1\omega, \Omega F_2)} \tag{3.10}$$

Where k is the turbulent kinetic energy, ω is the specific rate of dissipation. a_1 is a constant, Ω is the magnitude of vorticity, $\Omega = \sqrt{2W_{ij}W_{ij}}$, with vorticity defined as $W_{ij} = \frac{1}{2}(\frac{\partial u_i}{\partial x_j} - \frac{\partial u_j}{\partial x_j})$. Lastly, F_2 is defined as $tanh(arg_2^2)$, arg_2 is defined by the function $arg_2 = max(2\frac{\sqrt{k}}{\beta^*\omega d}, \frac{500\nu}{d^2\omega})$. The constant d is defined as the distance from the field to the nearest wall point and β^* is a constant.

The transport equations for turbulent kinetic energy, k, and specific dissipation, ω, are shown in equations (3.11) and (3.12), respectively [66].

$$\frac{D}{Dt}(\rho k) = P - \rho\beta^*\omega k + \frac{\partial}{\partial x_j}[(\mu + \sigma_k\mu_t) + \frac{\partial k}{\partial x_j}] \tag{3.11}$$

$$\frac{D}{Dt}(\rho\omega) = \frac{\gamma}{\nu_t}P - \rho\beta^*\omega^2 + \frac{\partial}{\partial x_j}[(\mu + \sigma_k\mu_t)\frac{\partial\omega}{x_j}] + 2(1-F_1)\frac{\rho\sigma_{\omega 2}}{\omega}\frac{\partial k}{\partial x_j}\frac{\partial\omega}{\partial x_j} \tag{3.12}$$

Where P represents the production of turbulent kinetic energy based on the shear stress of the flow, $P = \tau\frac{\partial u_i}{\partial x_j}$, $\tau = \mu_t(2S_{ij} - \frac{2}{3}\frac{\partial u_k}{\partial x_k}\delta_{ij} - \frac{2}{3}\rho k\delta_{ij}$, and, $S_{ij} = \frac{1}{2}(\frac{\partial u_i}{\partial x_j} + \frac{\partial u_j}{\partial x_i})$. $F1$ is a blending function, define by $tanh(arg_1^4)$, where, $arg_1 = min[max(\frac{\sqrt{k}}{\beta^*\omega d}, \frac{500\nu}{d^2\omega}), \frac{4\rho\sigma_{\omega 2}k}{CD_{k\omega}d^2}]$.For further information on the constant values and definitions the reader is referred to the `OpenFOAM` user guide[66],the work of Menter [39] or the NASA database for turbulence modelling resources [67].

The physically-inspired but empirically derived one equation SA model solves the following transport equation (3.13):

$$\frac{D}{Dt}(\tilde{\nu}) = C_{b1}\tilde{S}\tilde{\nu}(1-f_{t2}) - [C_{\omega 1}f_{\omega} - \frac{C_{b1}}{k^2}f_{t2}](\frac{\tilde{\nu}}{\tilde{d}})^2 + \frac{1}{\sigma}[\frac{\partial}{\partial x_j}((\nu+\tilde{\nu})\frac{\partial \tilde{\nu}}{\partial x_j}) + c_{b2}\frac{\partial \tilde{\nu}}{\partial x_i}\frac{\partial \tilde{\nu}}{\partial x_i}] \quad (3.13)$$

Equation 3.13 is solved for the term $\tilde{\nu}$, which is related to the turbulent viscosity by the set of equations (3.14)-(3.16).

$$\nu_t = \tilde{\nu} f_{v1} \quad (3.14)$$

$$f_{v1} = \frac{X^3}{X^3 + C_{v1}^3} \quad (3.15)$$

$$X = \frac{\tilde{\nu}}{\nu} \quad (3.16)$$

Furthermore, $\tilde{S} = \Omega + \frac{\tilde{\nu}}{k^2 d^2} f_{v2}$, where similarly to the $k-\omega$ SST model Ω is the magnitude of the vorticity. $f_{v2} = 1 - \frac{X}{1+X f_{v1}}$, $f_{\omega} = g[\frac{1+c_{\omega 3}^6}{g^6+c_{\omega 3}^6}]^{\frac{1}{6}}$, $g = r + c_{\omega 2}(r^6 - r)$, $r = min[\frac{\tilde{\nu}}{\tilde{S}k^2 d^2}, 10]$, $f_{t2} = c_{t3} exp(-ct4X^2)$. Constant values and further definitions of the above terms can be found in the `OpenFOAM` user guide[68], the original work by Spalart and Allmaras [69] or the NASA database for turbulence modelling resources [70]. The turbulence models are shown to emphasize the complex nature of turbulence modelling. However, they provide a simple turbulent viscosity, μ_t, for the approximation of the Reynolds stress using the shear stress tensor.

3.2 Compressible Transpiration Cooling Setup

In this section, the details of both the DNS and RANS simulations are presented. The objective is to provide a one-to-one comparison between the DNS and the RANS computations in order to carefully assess the near-wall turbulence modeling under transpiration blowing under strong wall-cooling conditions.

3.2.1 DNS database

In a previous contribution [27], we presented Direct Numerical Simulations (DNS) of spatially-evolving, transpired turbulent flat plate boundary layers. In the present work,

these simulations will serve as the basis to assess the near-wall modeling strategies within the context of Reynolds-averaged Navier-Stokes (RANS) solvers. Here, we summarize the main parameters of the DNS database; interested readers can consult the work of Christopher et al. [37] for further details and validation of the simulations.

The DNS was conducted using Hybrid [71] which solves the compressible and variable-viscosity form of the conservative Navier-Stokes equations. The mass, momentum, and energy equations are closed with the ideal gas law; the viscosity follows a power law with temperature. A sixth-order, central difference scheme was used for the spatial derivatives with a high-order filter to stabilize the central scheme. The time integration relies on a fourth-order explicit Runge-Kutta scheme using a CFL bounded time-step.

In these spatially-developing simulations, the turbulent boundary layer evolves from the inlet to reach a fully-developed state at a position approximately equal to 30 times the initial boundary layer height (δ_i) downstream; at this location, we impose the start of transpiration cooling at the wall. In the present work, we consider both the uniform blowing and the slit blowing cases. In the case of uniform blowing, we impose a uniform transpiration velocity directed normal to the surface in the transpiration region; this velocity corresponds to the Darcy velocity leaving the porous media. In the slit blowing cases, we alternate a repeating pattern of a transpiration strip (in the span) followed by a solid wall throughout the defined region of transpiration. For the slit cases, the transpiration region covers one third (by area) blowing slits whereas the other two thirds of the area is a cooled, isothermal wall. Here we consider the case of an array of 14 blowing strips. It should be noted that we force the same blowing ratios in both cases. The blowing ratio is defined as $F = \rho_c \mathbf{v}_w / \rho_\infty u_\infty$, where $\mathbf{v}_w$ is the average Darcy velocity of the injected flow over the transpiration region. For the uniform case, we impose a blowing ratio, F, equal to 0.2%, 0.6% and 2%; the cases correspond respectively to a low, medium, and high blowing ratio. For the slits case, we only consider the medium, and high blowing ratio cases (F = 0.6% and 2.0%) in the present work. Additionally, a case without any blowing (but with cooled walls) was computed as a baseline simulation and compared against published turbulent boundary layer simulations [37].

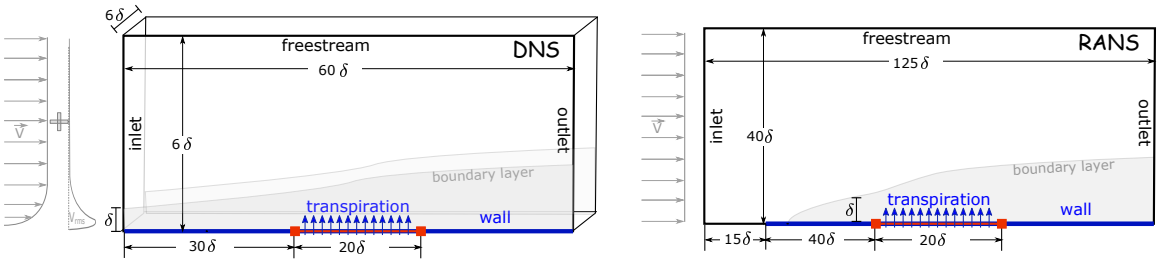

Figure 3.2 Illustration of the domain characteristics for the DNS (left) and RANS (right) simulations (not to scale).

Synthetic turbulence, with appropriate temporal and spatial correlation lengths, is superimposed over a time-averaged turbulent boundary layer profile at the inlet for all cases. Using proper scaling, the turbulence and mean velocity profile at the inflow are taken from the incompressible DNS database at $Re_\tau = 450$ by Jimenez et al. [72]. The freestream Mach number of all the cases in the present work is set to 0.3. The freestream and outflow boundaries use non-reflecting conditions supplemented by a sponge layer to dampen out the spurious numerical oscillations at the boundaries. Periodicity is assumed in the spanwise direction. To fully-resolve all the turbulence scales, about 118 million grid points were needed ($2560 \times 180 \times 256$), this guaranteed $y^+ \approx 1$ over the domain. The computational domain is scaled based on the inlet boundary layer thickness, δ_i, and is equal to: $L_x = 60\delta_i$, $L_y = 6\delta_i$, and $L_z = 6\delta_i$. The transpiration zone, for both the uniform and slits cases, has a $20\delta_i$ streamwise length between $x = 30\delta_i$ to $x = 50\delta_i$ to permit the unobstructed evolution of the turbulent boundary layer upstream and downstream of the transpiration region. For the slits case, the $20\delta_i$ transpiration zone is an alternating sequence of transpiration and solid wall regions, with solid wall comprising two thirds of the zone. Since the characteristic pore size in the transpiration zone is assumed to be much smaller than any of the turbulent length scales in the flow, we assume a no-slip condition on the streamwise velocity component at the wall. All the solid walls in the simulation are set to a fixed temperature of $T_w = 0.5T_\infty$, which is the same temperature as the injected flow in the transpiration region. These conditions correspond to strongly-cooled wall conditions. An illustration of the characteristic dimensions of the simulation are presented in Figure 3.2 (left). An instantaneous snapshot

at a fixed spanwise slice of two uniform and two slits DNS cases are shown, respectively, in Figures 3.3 and 3.4. As the DNS cases correspond to three-dimensional spatially and temporally varying simulations, the mean and turbulence statistics are averaged over a couple eddy turnover times and over the periodic dimension in the span once the initial transience in the flow is overcome. This permits adequate statistical convergence of the mean flow statistics. The validity of the first- and second-order statistics are assessed in the work of Christopher [37]. The methodology used in conducting these simulations, including initialization of the domain, the bounds of the statistically-steady turbulent state, and time integration can be found in the thesis of Christopher [37] as well.

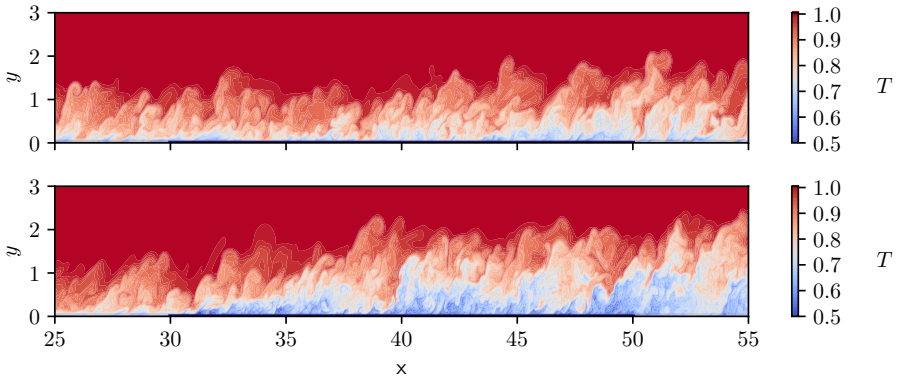

Figure 3.3 Instantaneous slice of the temperature distribution in the DNS uniform case at a blowing ratio of $F = 0.6\%$ (top) and $F = 2.0\%$ (bottom).

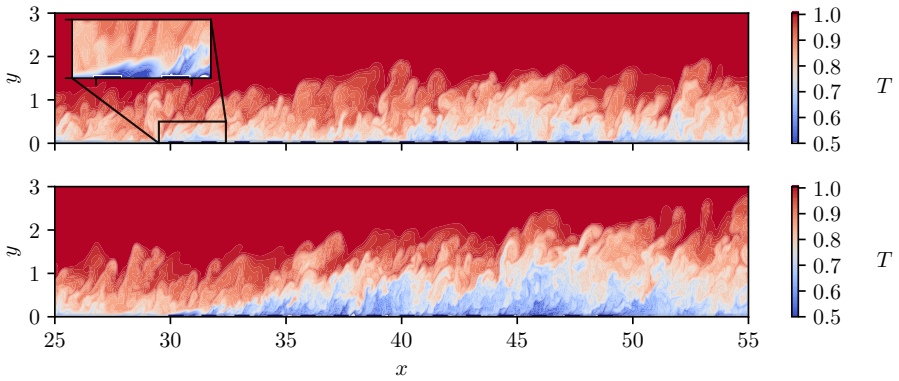

Figure 3.4 Instantaneous slice of the temperature distribution in the DNS slits case at a blowing ratio of $F = 0.6\%$ (top) and $F = 2.0\%$ (bottom).

3.2.2 RANS simulations

A set of comparative two-dimensional, Reynolds-Averaged Navier-Stokes (RANS) simulations are conducted using the rhoCentralFoam solver. Given the unsteady nature of the solver, the simulations were run until a steady-state is established. The simulation is setup to replicate all the salient operating conditions of the DNS, including its nondimensionalization. For the inflow condition, we impose a uniform velocity slightly upsteam of the start of the cooled flat plate; the boundary layer develops over the cooled solid wall ahead of the transpiration cooling section, see Figure 3.2 (right). The length of the cooled-wall ahead of the transpiration region is selected to allow the spatial development of the boundary layer such that it matches the boundary layer state at $x = 20\delta$ in the DNS. The similar turbulent statistics at the start of transpiration allow for a direct comparison between the DNS and RANS results. Outlet boundary conditions are imposed to the top and right boundaries; a cooled, isothermal, no slip wall (at $T_w = 0.5T_\infty$) is applied over most of the bottom boundary. The blowing ratio F is rigorously matched to the DNS, thus assuring that the same momentum is injected in the turbulent boundary layer. For both the uniform and slit cases, the injected transpiration flow is modeled as a Dirichlet boundary condition with a user-defined wall-normal velocity and temperature. The use of a plug-flow in the slit case differs slightly from the DNS which imposed a parabolic profile to the wall-normal velocity. It is noted that the blowing ratios are computed *a posteriori* through the integration of the density and velocity across the inlet and transpiration boundaries of the fully converged solution. The turbulence is modeled using the standard implementation of the Spalart-Allmaras (SA) for most of this work; an additional turbulence closure model is assessed later in this work.

The standard grid for the uniform simulations is 1000×450 grid points in the streamwise and wall normal directions, respectively, using a fully structured mesh; the slit cases have a slightly higher resolution as we need to accurately resolve the gradients at each of the 14 slits in the transpiration region. We set a grid clustering in the wall normal direction with a total expansion ratio set to 1000; a leading edge grid clustering approach was used in the streamwise direction. The grid resolution guaranteed that y^+ of the first grid point far below

unity over the entire domain (we recall that the Reynolds number is relatively low in order to match the DNS). Given the small computational cost of the RANS simulations, a number of cases have been run for comparative purposes although the comparison will focus on the similar blowing ratios as the DNS database.

The grid and domain size of the RANS simulations were first determined based on cooled wall case without transpiration and compared to the corresponding DNS. For this initial validation, we used the SA turbulence model and adjusted the length of the flat plate in order to match the boundary layer characteristics at the region of interest. It is important to note that, given the difference in the inflow conditions between the RANS and DNS, we set up our simulation by matching the boundary layer characteristics using the SA model. When studying the turbulence model effects, we only changed the modeling of the turbulence closure and did not attempt to match the boundary layer characteristics (for greater generalizability of our results). For all cases, given the unsteady solver, we assured that a steady state was reached. The steady state was assessed by a fixed coefficient of friction at the wall and an invariant temperature profile evaluated immediately downstream of the transpiration region. As the velocity and temperature profiles are resolved without the use of wall functions and we have very large temperature gradients. Non-physical, grid-to-grid temperature oscillations were sometimes observed, especially in the fine mesh cases, despite a small tolerance on the residuals (below 10^{-11} for most variables). These cases were discarded and re-run with slightly different initial conditions and tighter residual tolerances. This iterative approach was successful in obtaining physically consistent simulation results.

3.3 Shock Vector Control Setup

The simulations for the shock vector control study were split into two parts. The first set of simulations are used to validate the solver and are compared to the work of Gülhan and Braun [9] in Chapter 4. The second set of simulations are used to study SVC, and are analysed in Chapter 5. Both sets are equivalent in numerical details except the freestream inlet for the validation set is at a -5 degree angle of attack(AOA) relative to the flat plate

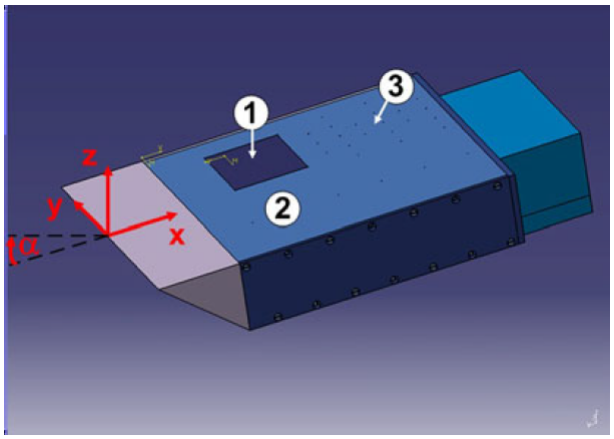

Figure 3.5 3D model of test apparatus used by Gülhan and Braun [9]

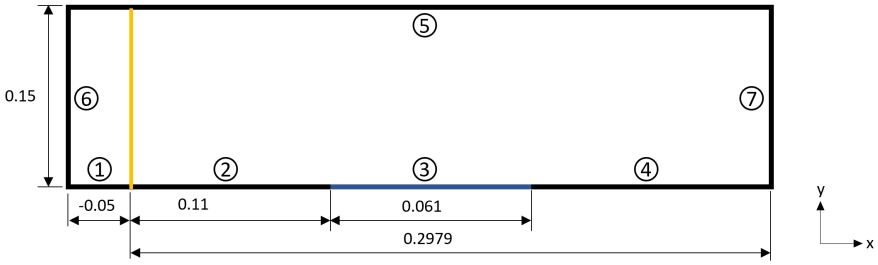

Figure 3.6 Schematic of computational domain used for SVC simulations

to match the experimental configuration of Gülhan and Braun [9]. For the transpiration cooling/SVC study, the AOA was set to 0.

3.3.1 Simulation Domain and Boundary conditions

The computational domain is set up to replicate the test apparatus used in experiments, see Figure 3.5. From this, a 2D approximation is used to model the air flow above the plate as the three-dimensional effects are of secondary importance. The overall domain size is $L_x = 0.3479m$, $L_y = 0.15m$ with 1 mesh element in the z direction. The overall domain schematic can be seen in Figure 3.6 with the numbered labels representing different boundary conditions. The test conditions of the freestream are given in Table 3.1, and the thermodynamic state (pressure and temperature) can be set exactly. The velocity

Free stream condition	Value
Free stream Mach number, M_∞ [-]	6
Free stream pressure, p_∞ [Pa]	380
Free stream temperature, T_∞ [K]	89
Free stream density, $\rho_\infty[K/m^3]$	0.01487
Dynamic pressure, q [Pa]	9,576
Total temperature, T_0 [K]	730
Total pressure, p_0 [Pa]	$6x10^5$
Reynolds number, $Re[-]$	$0.73x10^6$

Table 3.1 Free stream conditions in experiments run by Gülhan and Braun [9]

components can be calculated by first calculating the speed of sound for air at the given conditions. Next, the speed of sound is multiplied by the Mach number to obtain the speed of the air. Due to the 5 degree angle of attack of the wedge, trigonometric functions are used to find the components of velocity in the x and y direction. The remainder of the boundary conditions were found from temperature distribution figures in the original work, no-slip wall conditions and trial and error. The prescribed boundary conditions for the case corresponding to the work of Gülhan and Braun [9] are organized in Table 3.2.

At the surface of the porous media there are a series of microscopic solid walls and openings alternating in a non-uniform pattern. At the wall segments, a no-slip condition must be present. However, over the openings, the velocity in the x-direction is free to be any value, at least mathematically. Due to a lack of experimental and analytical models, the correct slip velocity in the x-direction at the wall is not known. Running simulations that incorporated every pore would be too computationally expensive to complete. Currently, two techniques are used by modellers for commercially available CFD codes to approximate the transpiration x-velocity. The first is to assume the pores are large channels of injectant into the flow and the remainder of the region is modelled by a no-slip condition as done by Prokein et al. [38] (circular pores) and Christopher et al. [27] (channel slits). This

Boundary Condition Number	X-velocity [m/s]	Y-Velocity [m/s]	Pressure [Pa]	Temperature [K]
1: Entrance length	1130.40	-98.89	$\frac{\partial p}{\partial y} = 0$	$\frac{\partial T}{\partial y} = 0$
2: Upstream wall	0	0	$\frac{\partial p}{\partial y} = 0$	335
3: Transpiration region	0	10.58	$\frac{\partial p}{\partial y} = 0$	310
4: Downstream wall	0	0	$\frac{\partial p}{\partial y} = 0$	Q=7250 W/m
5: Top boundary	1130.40	-98.89	$\frac{\partial p}{\partial y} = 0$	89
6: Inlet	1130.40	-98.89	380	89
7: Outlet	$\frac{\partial u}{\partial x} = 0$	-	$\frac{\partial p}{\partial x} = 0$	$\frac{\partial T}{\partial x} = 0$

Table 3.2 Boundary condition values

Case	Simulation name	Notes
1	F=0	Transpiration velocity set to zero
2	F=0.444	
3	F=0.874	This is the baseline case
4	F=1.000	
5	F=1.500	
6	F=2.000	
7	F=0.874 Mach 5	Identical to 3, but freestream Mach number is 5
8	F=0.874 Mach 7	Identical to 3, but freestream Mach number is 7
9	F=0.874 entrance x05	Identical to 3, but the upstream plate length is halved
10	F=0874 entrance x2	Identical to 3, but the upstream plate length is doubled
11	F=0874 turbulent	Identical to 3, but $k - \omega$ SST used to model turbulence

Table 3.3 Details of SVC cases

Case	Simulation name	Mesh size(x,y)
1	Very coarse mesh	446x109
2	Coarse mesh	892x275
3	Baseline mesh	1783x436
4	Fine mesh	1783x872

Table 3.4 Details of SVC validation cases

method works well, however, introduces oscillations in flow quantities due to larger pore sizes. Alternatively, the whole domain can be modelled as a no-slip condition as done by Christopher et al. [27]. The flow quantities do not have large oscillations present but the mixing is exaggerated due to a full no-slip condition. For the current work a no-slip boundary condition is applied to the x-velocity over the transpiration region. It will be shown in Chapter 4 that the boundary layer is similar to that of experiments but slightly larger. The idealization of the transpiration boundary condition should be kept in mind throughout this work.

The validation cases are organised in Table 3.4 by mesh size and are identical in all other respects.

3.3.2 Simulated cases

The simulated cases are highlighted in Table 3.3. The first set of cases (1-6), explore the cause and effect of altering the velocity of fluid injectant. While, cases 7-11 are identical to case 3 but altered some of the flow variables. For all cases the injected transpiration fluid is at 295K, the upstream wall has a Dirichlet boundary condition of 335K and the downstream wall has a Neumann boundary condition specifying the heat flux at the wall which is the same as in Table 3.2 . The blowing ratio is defined as $F = \overline{\rho}_c \mathbf{V_c} / \overline{\rho}_\infty U_\infty$ where $\mathbf{V_c}$ is the Darcy velocity, defined by equation (3.17).

$$\mathbf{V_c} = \frac{1}{x_b - x_a} \int_{x_b}^{x_a} V dx \tag{3.17}$$

Where x_a and x_b are the beginning and end of the transpiration region, respectively. It should be noted cases 7-11 do have an exact blowing ratio of 0.874, this is a naming convention used to identify cases 7-11 as almost identical to case 3.

Chapter 4

Validation

This chapter will focus on validating the two distinct set of simulations outlined in chapter 3. A mesh refinement study was done for the compressible transpiration cooling simulations in section 4.1. The subsequent section will be divided into three subsection to validate the hypersonic simulations.

4.1 Compressible transpiration validation

Given the very strong thermal gradient at the wall, the grid sensitivity is carefully assessed. For the DNS database, the readers are referred to the original publication [27] and thesis [37] work which contain grid sensitivity studies on the second-order turbulence statistics. For the RANS simulations, Figure 4.1 shows the grid sensitivity of the temperature, velocity, and eddy viscosity for three grid resolutions: coarse (500×225), baseline (1000×450), and fine (1414×636). The sensitivity study is conducted on the highest blowing ratio case ($F = 2.0\%$).

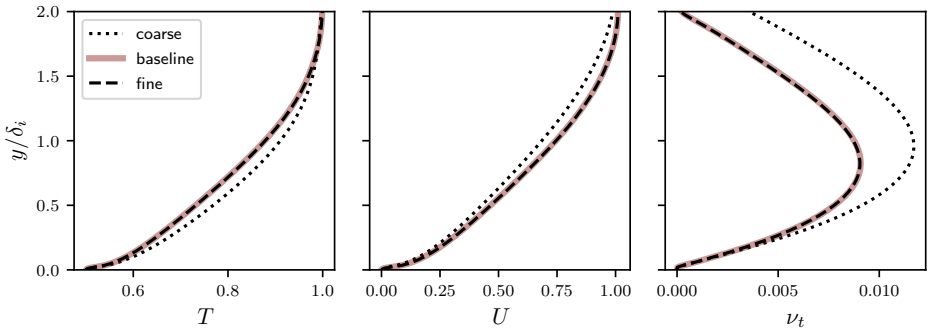

Figure 4.1 Sensitivity of the key variables at mid-point in the transpiration zone $x = 41\delta_i$ for the highest blowing ratio case ($F = 2.0\%$, uniform) on a coarse (500×225), baseline (1000×450), and fine (1414×636) grid.

4.2 Shock Vector Control Simulations

4.2.1 Grid Convergence

Grid convergence was extensively studied, especially at the near wall regions and across shocks in the flow domain. The names and sizes of the tested meshes were: very coarse mesh (446x109), coarse mesh (892x275), baseline mesh (1783x436) and fine mesh (1783x872). The x-momentum and temperature profiles were compared between each case, in multiple locations. A few examples can be seen in Figure 4.2, upstream, in the middle and downstream of the transpiration region. Subfigures a), b) and d) show a good agreement between all mesh configurations. However, when looking at subfigure c), it is evident that the two coarse mesh configurations are not fine enough to capture the flow physics. The baseline mesh and fine mesh overlap at all instances. Further refinement was tested but no difference was observed.

By definition, the transpiration velocity,$\mathbf{V_c}$, is the integration of all velocities along the transpiration domain as given by equation (3.17). However, a value for the transpiration velocity is only available at every node along the wall. The trapezoid rule is used to

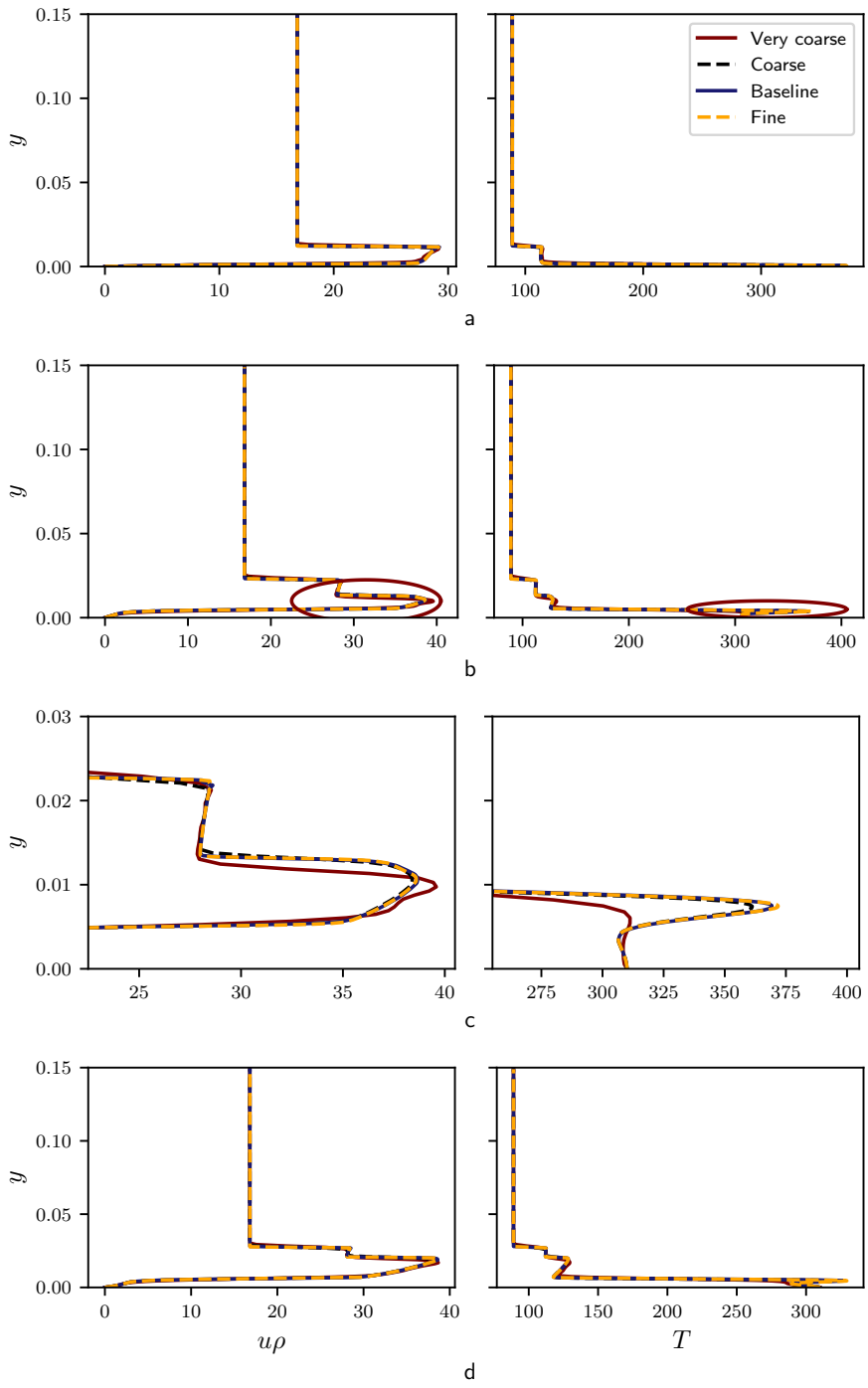

Figure 4.2 X-momentum and temperature profile of: a) upstream of transpiration(x=0.07) b) middle of transpiration(x=0.14) c) Middle of transpiration, region enlarged to view small discrepancies as shown by red ovals d) downstream of transpiration(x=0.17)

Mesh size	Blowing ratio
Very coarse (446x109)	0.874
Coarse (892x275)	0.845
Baseline (1783x436)	0.848
Fine (1783x872)	0.848

Table 4.1 Comparing the blowing ratio versus the mesh size

approximate the velocity integral as given by equation (4.1).

$$\int_{x_b}^{x_a} V dx \approx \sum_{n=1}^{N} \frac{V(x_{k-1}) + V(x_k)}{2} \Delta x_k \tag{4.1}$$

Applying this method to each mesh yields the resulting blowing ratios as seen in Table 4.1. The coarse and very coarse mesh are not fine enough to capture the flow physics as accurately as desired. A similar conclusion to that of the study summarized in figure 4.2 is reached and the baseline mesh is chosen.

4.2.2 Time Convergence

The solver used to model the flow is an unsteady solver, however, to analyze the flow the steady state condition is desired. To conclude the simulation has reached a steady state, it must be demonstrated that the solution does not change with time. Due to the inherent instability of the shock wave, there are small fluctuations in the flow. For better comparison, after the simulation reached a state where no change was present except for the repeating waves, the data was averaged over 2 plate flow through times for comparison. A plate flow through time (FTT) is defined as time needed for the freestream flow to travel the length of the plate, as is defined by equation (4.2).

$$t_{FTT} = \frac{L_x}{V_\infty} \tag{4.2}$$

The results of the time convergence study can be seen in Figure 4.3, using the baseline mesh and comparing the temperature profile in the middle of the transpiration region at different

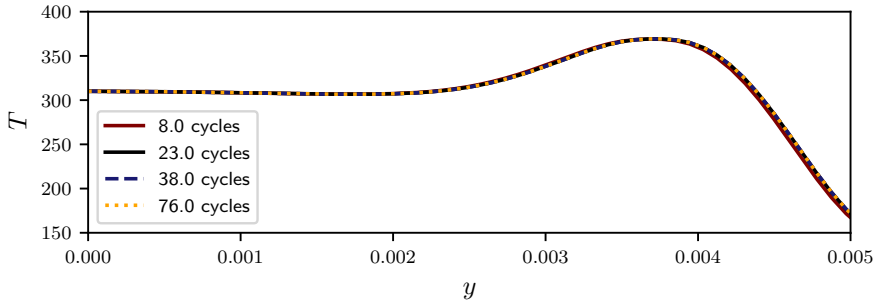

Figure 4.3 Time-averaged temperature profile (flow-through time $t_{FTT} = 2.6E-4$)

moments in time. The results show that after 8 flow through times, the simulation still shows transience from $y = 0.004$ to $y = 0.005$, as the temperature profile undershoots all other profiles. After, 23 flow through times is where the flow can be said to have reached a steady state. To introduce a safety factor, it was decided to run all future cases to 38 flow through times. The chosen quantity for the time convergence study was temperature, due to it having the largest error in the grid convergence study. However, the same trend held when other quantities we used for the time convergence study.

4.2.3 Experimental Comparison

To validate the simulated results, we first compare the angle of the shock waves between the experimental and simulated cases. The only description of shock wave angles by Gülhan and Braun [9], was in a figure showing a Schlieren image of the flow. A common method for approximating Schlieren images is to plot the $|\nabla\rho|$ on a plane surface[73]. The $|\nabla\rho|$ field was computed and overlaid the Schlieren image of Gülhan and Braun [9] in Figure 4.4. The angles of the leading shock wave align with the experimental and simulated results, labeled 2. The simulated separation shock wave has a higher angle; 42 versus the experimental angle of 39 calculated from the flat plate, labeled 5. This mismatch is due to the larger simulated boundary layer height. As the boundary layer protrudes further into the main flow, the hypersonic flow must be deflected further upward resulting in a higher angled shock wave. It is not possible to resolve this issue due to the following two competing

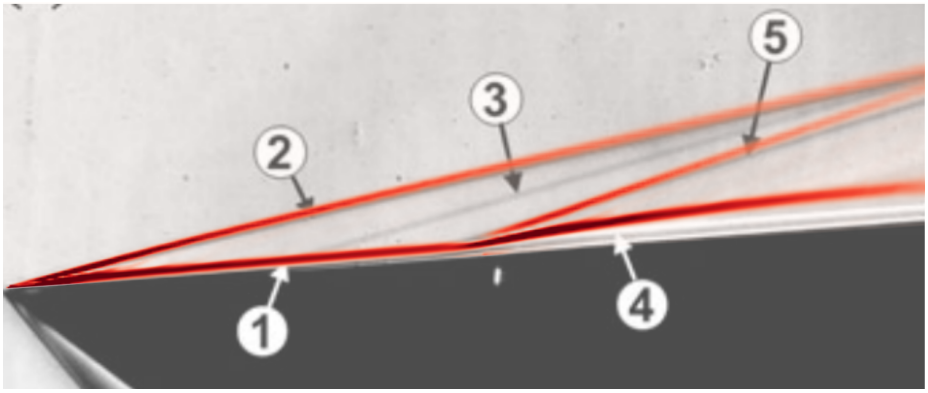

Figure 4.4 Comparison of experimental(gray scale) and simulated (red) Schlieren image[9]

factors: the prescribed blowing ratio and the no-slip condition throughout the transpiration region. As will be demonstrated in the following sections, as the blowing ratio is increased, the boundary layer height will also increase. The no-slip condition at the wall imposes a strict zero velocity, causing boundary layer growth. The opposite condition would be an Euler wall, where the fluid velocity would not be slowed down by the wall and a boundary layer would not exist. The physical reality of a porous material is somewhere in between, as solid surfaces act like walls and porous openings act as a Euler wall.

The most obvious mismatch can be seen at label 3, and is classified as an interference shock by the authors. The interference shock is not explained at all in the paper by Gülhan and Braun [9]. But, it seems to be a result of different materials coming together, as shown by a solid model in the paper by Gülhan and Braun [9], and a picture of a similar fixture used by Gülhan [10] in other experiments - both are shown in Figure 4.5. In my work, I did not model the plate as an assembly of materials and therefore the interference shock wave does not appear. The reasons included for modelling the plate as one solid piece are: reduces model complexity, reduces run time, and accounting for different materials upstream would not help in the physical understanding of the flow in terms of SVC.

Lastly, the plate temperature will be compared to validate the accuracy of the solver. The boundary conditions were described by Figure 3.6 and Table 3.2. The measured temperature distribution can be seen Figure 5 in the work of Gülhan and Braun [9]. As mentioned, the upstream plate has a fixed temperature of 335K. This compares well to the

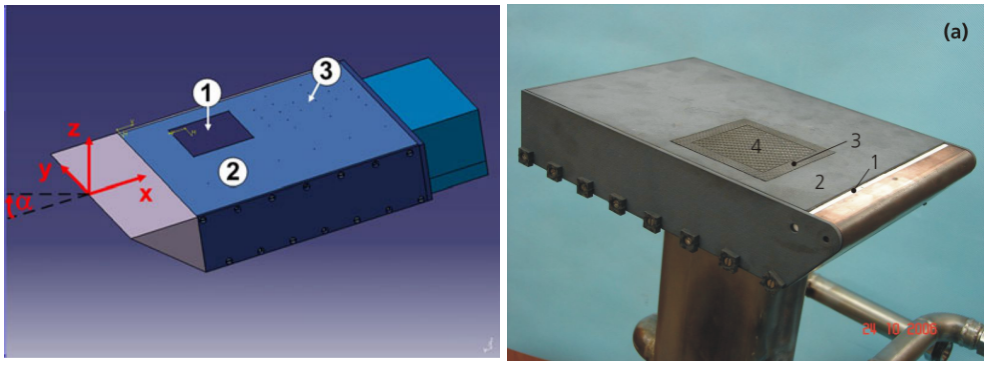

Figure 4.5 Solid model of experimental fixture done by Gülhan and Braun [9] (left), photo of similar fixture used in experiments by Gülhan [10].

experimental results as no temperature change is visible. Similarly, the experimental results for the transpiration region are uniform, except for small discrepancies near the transpiration boundaries, and compare well to the imposed value of 310K. Lastly, the downstream wall was much harder to model as the temperature has a non-linear increase down the plate. For this reason, the plate must be modelled with a heat flux condition imposed on the downstream plate. The difficulty is selecting an appropriate value due to the changing temperature gradient along the downstream wall. For this reason, an iterative approach was chosen where the average calculated heat flux was first selected and subsequently modified to achieve the most realistic results. The resultant temperature distribution of the wall can be seen in Figure 4.6. The orange vertical bars represent the range of possible values given by reading the colour map in the work of Gülhan and Braun [9]. The temperature comparison downstream of transpiration seems to indicate that the simulation reasonably models the experiments and can be used to study SVC parametrically.

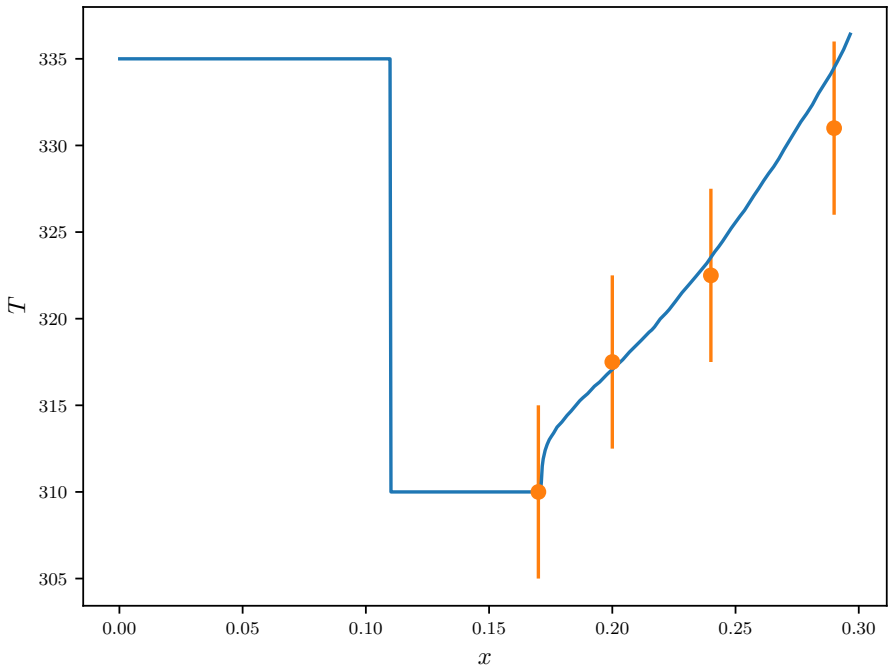

Figure 4.6 Simuated plate temperature profile (blue) overlaid with experimental data (orange) from Gülhan and Braun [9].

Chapter 5

Results and Discussions

5.1 Compressible transpiration results

The comparative results are discussed in this section. First, we assess the evolution of the mean flow properties in the transpiration cases at various blowing rates; for all these initial comparisons, the standard Spalart-Allmaras (SA) model is selected. Thereafter, the turbulence modeling in these cases are assessed and compared.

5.1.1 Evolution of mean flow statistics

The evolution of the near wall velocity profile, at discrete streamwise locations, and the evolution of the boundary layer thickness for the various uniform blowing cases is shown in Figure 5.1. This offers a direct comparison of the DNS and RANS results. For this comparison, the standard SA turbulence model is selected for the RANS calculations. Compared to the DNS, the boundary layer growth rate of the uniform RANS simulations is slightly over-predicted, which is attributable to a stronger turbulence production over the transpiration region, discussed in section 5.1.2. The overall qualitative evolution of the velocity profiles and boundary layer growth is well captured by the RANS solver. The velocity profiles at the start, mid-point, and slightly downstream of the end of the transpiration zone are overlaid in Figure 5.2. Importantly, the RANS solver captures the

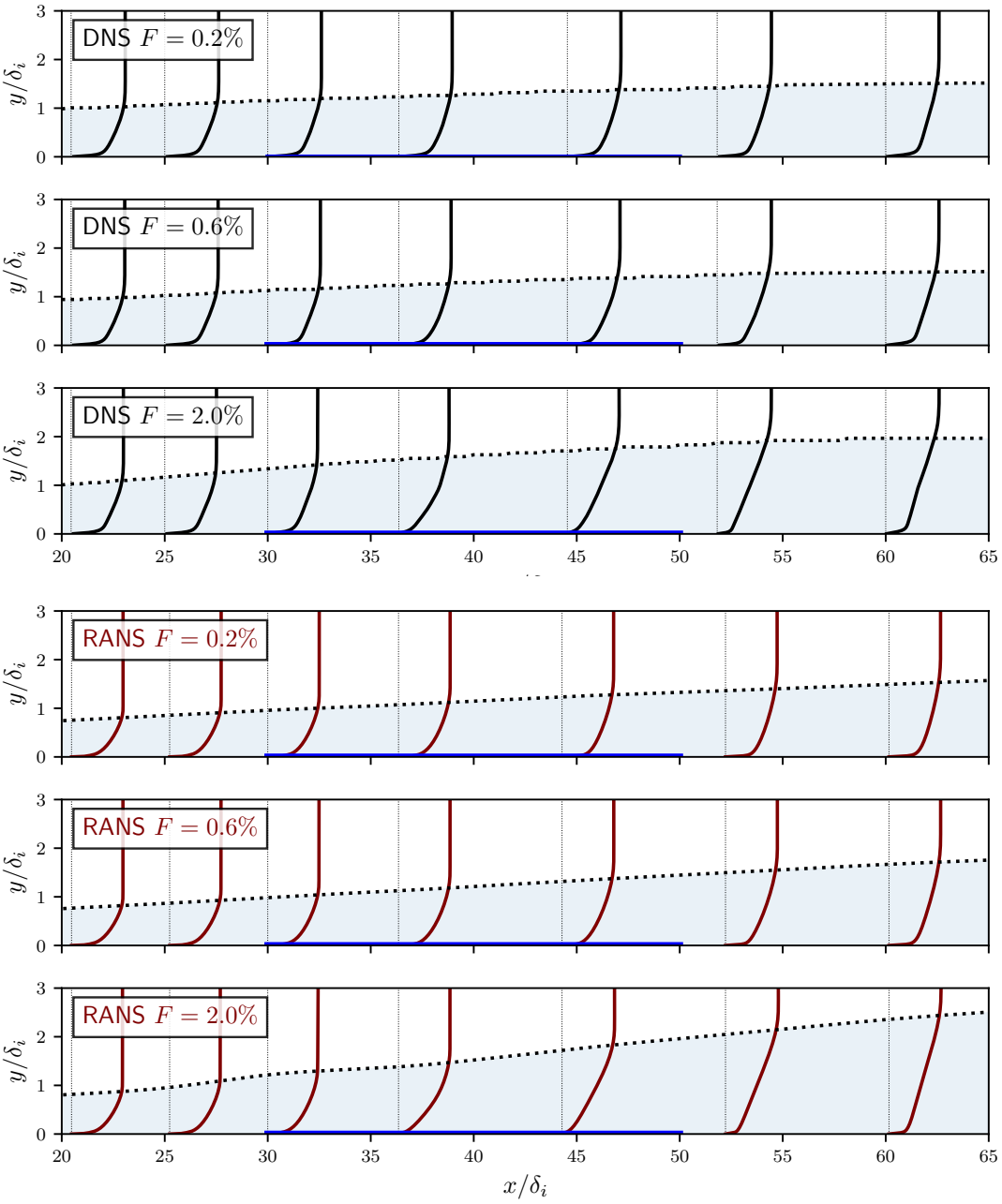

Figure 5.1 Evolution of the streamwise velocity profiles and boundary layer thickness. The region of transpiration cooling is identified at the wall with a dark blue line.

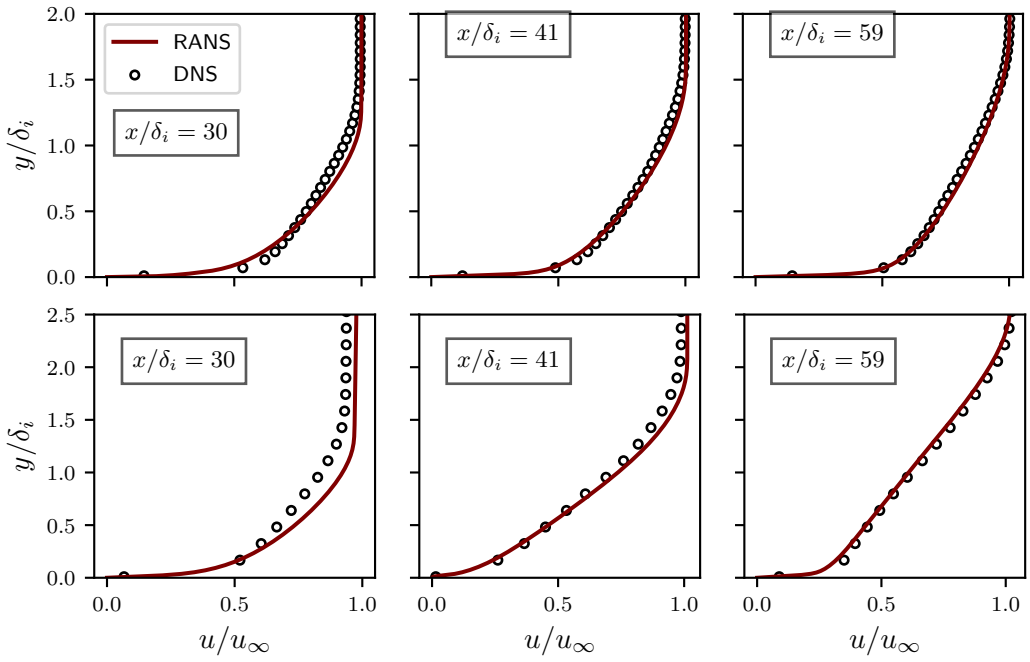

Figure 5.2 Velocity profiles of the RANS and DNS for $F = 0.2\%$ (top) and $F = 2.0\%$ (bottom) at the start (left), mid-point (middle), and downstream (right) for the uniform transpiration zone.

correct change in slope with increasing blowing ratio in the outer part of the boundary layer. The largest discrepancy is observed at the start of the transpiration region ($x/\delta_i = 30$). Within the transpiration zone ($x/\delta_i = 41$), both the low- (top) and high-blowing (bottom) ratios correctly account for the effect of the wall-normal momentum transport resulting from transpiration. Similarly, the aggregate effects of transpiration are accurately captured downstream of the transpiration zone at ($x/\delta_i = 59$).

The validation cases, without transpiration, showed a nearly perfect collapse of the evolution of the momentum thickness-based Reynolds number between the RANS and DNS simulations (not shown). The RANS simulations start to depart from the DNS results when the blowing ratio is non-zero. Figure 5.3 shows the comparison of the evolution of the momentum-thickness-based Reynolds number, Re_θ, and the shape factor, H for the uniform case. As expected, we note a drop in the momentum thickness over the transpiration region for the blowing ratios of $F = 0.6$ and 2.0% as the injected momentum into the boundary layer (resulting in a reduction of the momentum defect) overcomes the usual increase in

momentum thickness with streamwise evolution. At the lowest blowing ratio ($F = 0.2\%$), both the RANS and DNS show a monotonic increase in the momentum thickness through the transpiration region, although we note that the RANS results shows a stronger growth in the momentum thickness above the transpiration region. The high-blowing ratio case deserves specific consideration. Over the transpiration region, the drop in the momentum thickness in the RANS simulation is significantly greater than that of the DNS despite the moderate difference, at least qualitatively, in the velocity profile at these locations (recall Figure 5.2). Thus, we expect the thermodynamic effects, through the density term, to be responsible in compounding the error in the momentum thickness in the RANS.

The evolution of the shape factor is shown in Figure 5.3 (right). The shape factor represents the ratio of the displacement, δ_2, to the momentum, θ, thickness and is defined as:

$$H = \frac{\delta_2}{\theta} = \frac{\int_{y=0}^{\infty} \left(1 - \frac{\rho u}{\rho_\infty u_\infty}\right) dy}{\int_{y=0}^{\infty} \frac{\rho u}{\rho_\infty u_\infty} \left(1 - \frac{u}{u_\infty}\right) dy} \tag{5.1}$$

A value of $H \approx 1.3$ is typical of incompressible, adiabatic turbulent boundary layers [74]. In the strongly-cooled turbulent boundary layer, the displacement thickness is expected to be smaller as higher density fluid is located close to the wall; this functional relationship between the shape factor and wall temperature can be seen in the analytical derivations by Standen [75]. A similar observation can be gleaned from the conditionally-averaged velocity profiles over heated and cooled wall segments in work by Hickey et al. [76]. If we do not account for the density change in the computation of H (thus computing the incompressible shape factor), we obtain a value of about $H \approx 1.57$ at $x/\delta_i = 30$. Clearly, the strong cooling greatly impacts the shape factor calculation, as shown in the results of the RANS and DNS. At low- and medium-blowing ratios ($F = 0.2$ and 0.6%), the shape factor decreases over the transpirative region as the displacement thickness decreases more rapidly than the momentum thickness. For the higher blowing ratio ($F = 2.0\%$), the large wall-normal blowing velocity effectively pushes the boundary layer away from the wall. This results in a faster decrease of the momentum compared to the displacement thickness. Thus we note a significant peak in H in the DNS which is also captured by the RANS,

although the magnitude and position of the peak differ between the simulations.

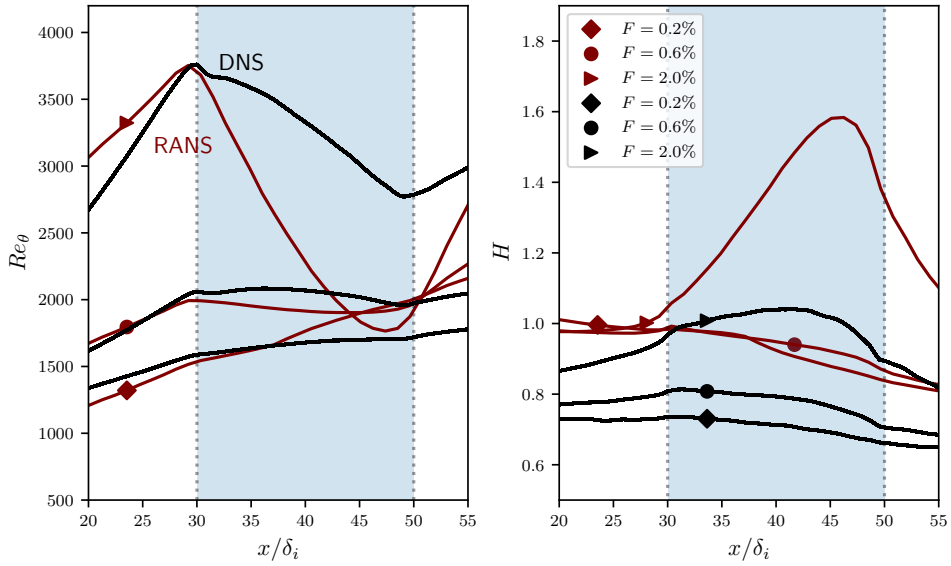

Figure 5.3 Evolution of momentum thickness Reynolds number (left) and shape factor (right) for the uniform cases.

Although the velocity profiles and integral boundary layer characteristics are important indicators for transpiration cooling, ultimately it is the temperature distribution that is of critical importance for thermal protection systems. Furthermore, given the zero-pressure-gradient turbulent boundary layer under consideration, the temperature distribution directly affects local density of the flow which, in turn, affects the velocity distribution through the conservation of mass. The temperature distribution over the transpiration region is shown in Figure 5.4 for the uniform simulations. At a given blowing ratio, the RANS simulations closely match the temperature distributions of the DNS, the match is especially good close to the wall. Farther away from the wall, in the outer edge of the boundary layer, the RANS simulations consistently under-predict the thermal mixing. This is an unexpected result given that the RANS results over-predicted both the boundary layer thickness and, as we will see in the next section, the turbulence stresses.

The direct comparison of temperature distribution in the slit case is shown in Figure 5.5. In order to have the same mass flow rate injected into the boundary layer (in order to match

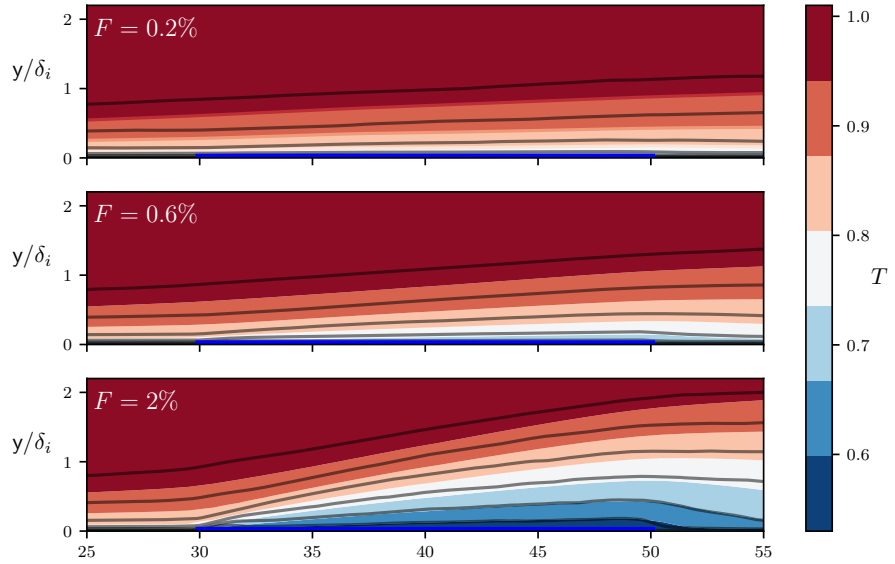

Figure 5.4 Comparison of the temperature distributions of the transpiration region for the uniform setup. RANS (SA model) results are shown with colored contour plot which is overlaid with the DNS results (at the same contour levels). The transpiration region is indicated with a blue line.

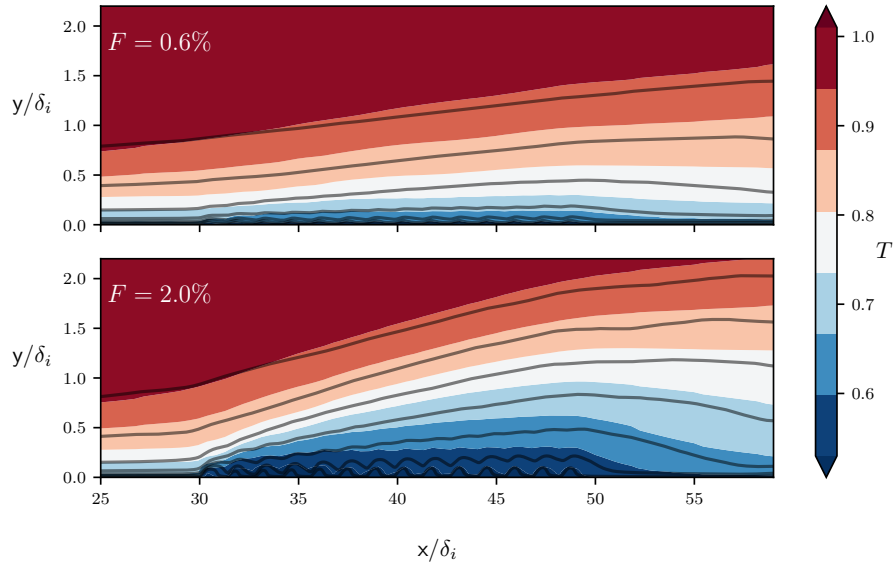

Figure 5.5 Average temperature for the $F = 0.6\%$ (top) and 2.0% (bottom) cases for the slits configuration. RANS (SA model) results are shown with colored contour plot which is overlaid with the DNS results (at the same contour levels).

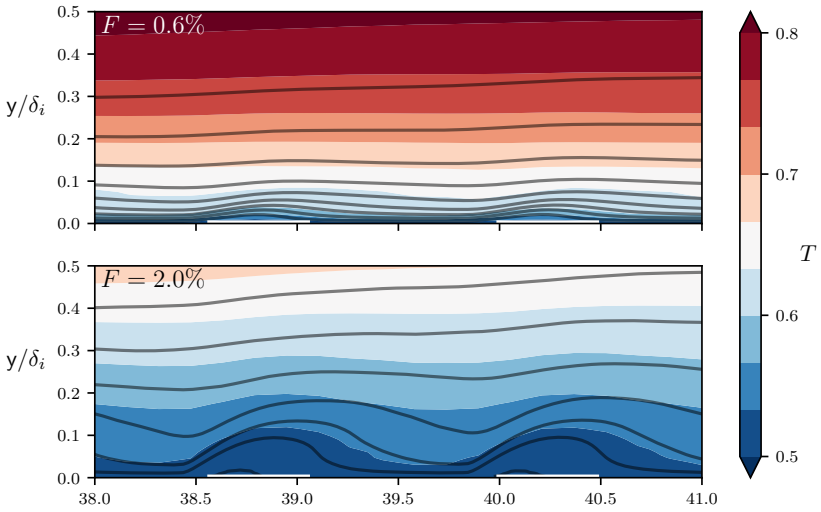

Figure 5.6 Focus on the average temperature distribution of the 7th and 8th opening in the slit case. Case $F = 0.6\%$ (top) and 2.0% (bottom). RANS (SA model) results are shown with colored contour plot which is overlaid with the DNS results (at the same contour levels). The opening at the wall is shown with a white line.

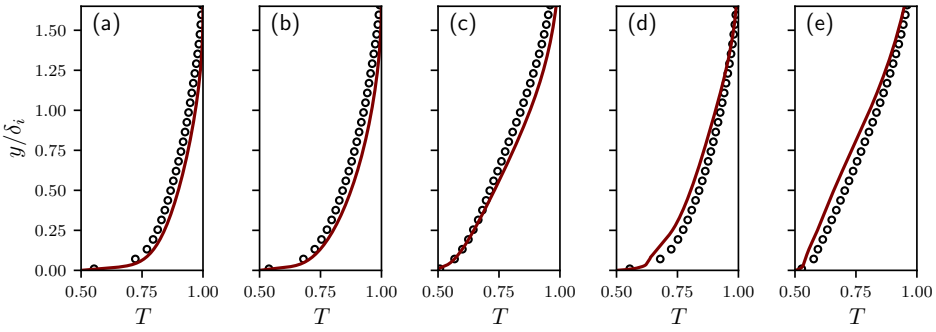

Figure 5.7 Temperature profile (DNS=symbols, RANS=line) at a single streamwise location near the mid-point of the transpiration region ($x = 41\delta_i$) for the cases: (a) $F = 0.2\%$ (uniform), (b) $F = 0.6\%$ (uniform),(c) $F = 2.0\%$ (uniform), (d) $F = 0.6\%$ (slits), (e) $F = 2.0\%$ (slits).

the blowing ratios), slit cases have a larger Darcy velocity compared to the uniform cases as only one third of the area of the transpiration region has openings; the remaining 2/3 of the transpiration region (defined from $x/\delta_i = [30, 50]$) consists of cooled walls. At both medium- and high-blowing ratios, we note a good collapse of the temperature distribution. Unlike the uniform configuration, the slit configurations shows a greater thermal mixing in the RANS, especially in the outer boundary layer. The growth rate of the thermal boundary layer is notably larger than the DNS over the transpiration region. Figure 5.6 focuses on the 7th and 8th blowing slit. Although Figures 5.4-5.6 provide an overview of the temperature distribution, a quantitative comparison of the temperature profile at $x = 41\delta_i$, for all cases, is shown in Figure 5.7. We note that the thermal gradient in the DNS, especially just above the entrance of the blowing sections, are not captured in the RANS. The RANS simulation shows a greater thermal mixing which is likely caused by the modeling approximations of the thermal flux (discussed later). This alternating sequence of wall and blowing represents a particularly challenging test case for all turbulence models. We do acknowledge a notable difference in the RANS and DNS setups for the slits cases. In the DNS, the wall-normal velocity in each slit follows parabolic velocity distribution, a similar velocity distribution was not used in the RANS which can result in differences in the momentum and thermal mixing.

To assess the effect of transpiration on the heat transfer at the wall, Figure 5.8 shows the evolution of the normalized thermal gradient at the wall for the uniform configuration, where the blue overlay is the area above transpiration region. Here, to facilitate the comparison, the normalization is done with respect to temperature gradient at $x/\delta_i = 25$. The drop in temperature gradient over the transpiration region as a function of the blowing ratio is well captured, even in the strong blowing case where the temperature gradient approaches zero. One notable discrepancy lies in the post-transpiration region in which the RANS simulations under-predict the temperature gradient. This post-transpiration region ($x/\delta_i > 50$) is characterized by the accumulation effect of the effused coolant immediately adjacent to the cooled wall. Thus, this result suggest that the aggregate accumulation effect may be over-predicted (or, alternatively, that the thermal flux at the wall is under predicted) in RANS

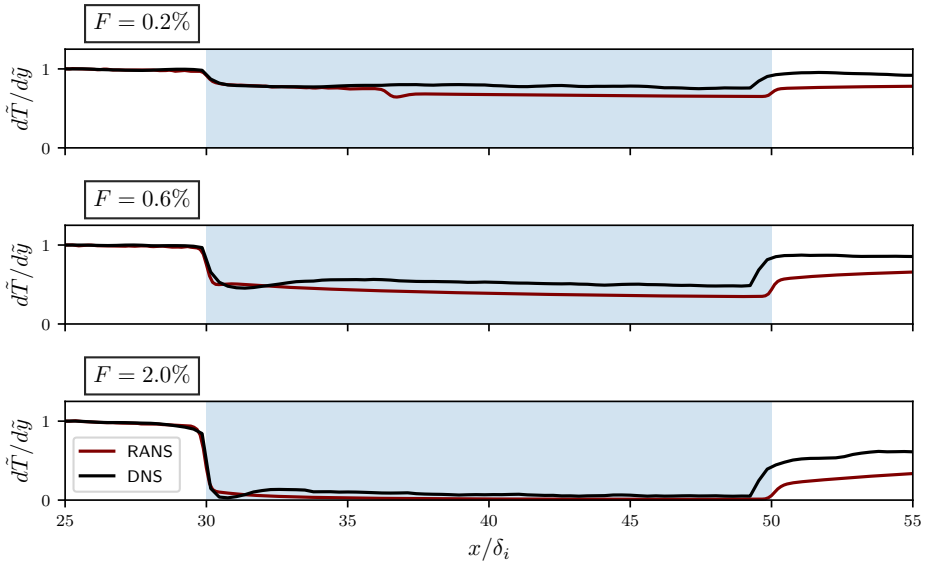

Figure 5.8 Normalized temperature gradient at the wall for the uniform cases. The values are normalized with the temperature gradient at the wall at $x/\delta_i = 25$.

calculations. This is possibly due to incorrect modeling of the turbulence-driven thermal flux, as observed in previous results and discussed in subsection 5.1.2. The normalized temperature gradient at the wall for the slits case is shown in Figure 5.9. Although the temperature gradient is well captured by the RANS, a very sharp change in the temperature gradient arises on the wall segment after each transpiration slit. The amplitude of the oscillations of the thermal gradient is not captured by RANS. This observation is confirmed by figure 5.6 showing the temperature distribution near the wall. Compared to the uniform case, the slit case shows better modeling of the accumulation effect in the post-transition region.

5.1.2 Turbulence modeling

Turbulence models play a key role in engineering-level predictive simulations of transpiration cooling. The turbulence strongly effects the mass, momentum, energy transfer and mixing, its impact is especially important above the transpiration zone which is characterized by high anisotropy. Therefore, it is important to assess the ability of standard turbulence

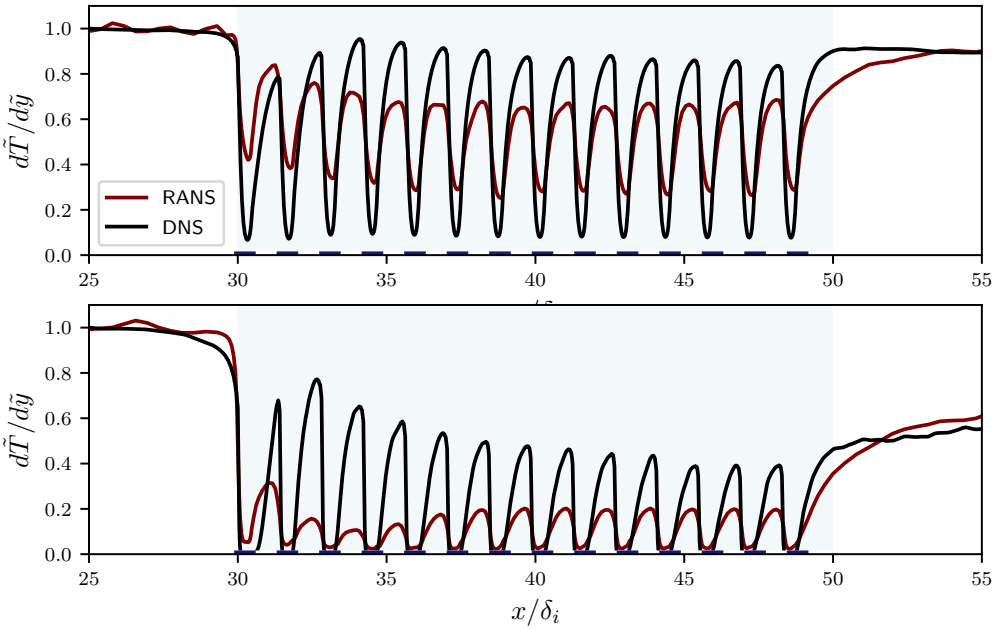

Figure 5.9 Normalized temperature gradient at the wall for the slit cases. The values are normalized with the temperature gradient at the wall at $x/\delta_i = 25$.

closure models to capture the turbulent statistics near the wall. Although experimental validations are important, few experiments report the higher-order turbulence statistics above the transpiration region. Often validations must rely on matching integral quantities in the flow. Here, since we have a spatio-temporally resolved turbulent boundary layer with transpiration, we can directly assess the RANS turbulence models against the DNS results. Despite the low-Reynolds number of the cases under investigation (due to the computational costs of our DNS), the Reynolds number remains sufficiently high to offer valuable insight into the modeling.

Here, we look at two very standard turbulence models, namely: Spalart-Allmaras (SA) and the Shear Stress Transport (SST). The SA model is a one-equation turbulence model. Although the SA turbulence model is decidedly more empirical than the standard two-equation models (such as $k-\epsilon$ or $k-\omega$), it generally has excellent predictive capabilities in zero-pressure gradient turbulent boundary layers[69]. The SST is a two-equation turbulence model that uses a blending function to optimize the strengths of both the $k-\epsilon$ and $k-\omega$ models near the wall. This represents one of the most versatile turbulence models and is often the default choice for engineering applications[77]. Many works propose corrections to these models (e.g. [29]) to account for the influence of wall normal flow and roughness; here the assessment is done on the standard formulations as implemented in OpenFoam.

When scaled with the near-wall characteristics, the velocity profiles show a modest difference at the middle (left) and downstream of the transpiration region (right) as in Figure 5.10. Both turbulence models correctly capture the viscous sublayer and most importantly the velocity gradient at the wall. The discrepancy arises within the buffer layer. On the cooled walls without transpiration ($x/\delta_i = 59$, right), both models show an identical slope in the log-layer despite a small offset of the curves. In the transpiration region ($x/\delta_i = 41$, left), the SST model shows a steeper slope compared to the SA model. This results in a better match of the boundary layer thickness of the SST model over the transpiration region (not shown).

The turbulent viscosity, which is computed from the turbulence transport equations, shows a non-negligible difference in the profile as seen in Figure 5.11 for the uniform

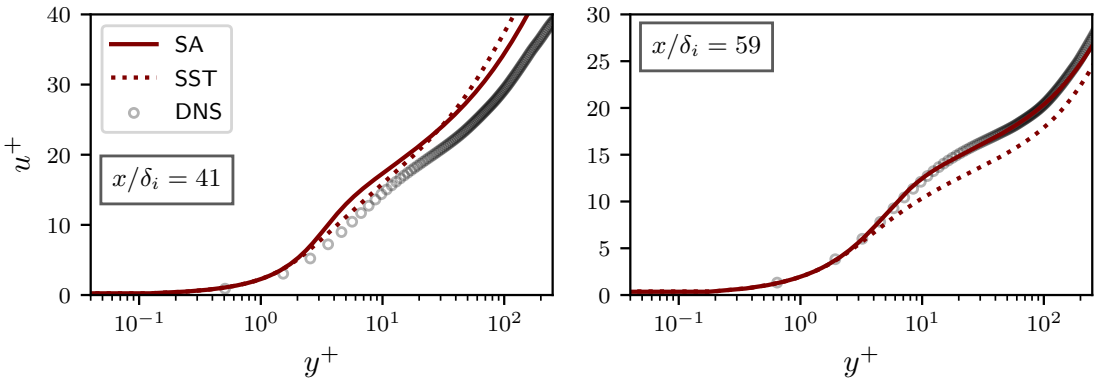

Figure 5.10 Turbulence models on the velocity at the middle ($x = 41\delta_i$, left) and downstream of the transpiration zone ($x = 59\delta_i$, right) for the uniform case at $F = 0.6\%$. Classical near wall scaling is used for all cases.

cases. The magnitude of the eddy viscosity peak differ by 50% and the range of non-zero turbulence fluctuations is greater in the SA model. As we have access to the full turbulence statistics in the DNS, we can assess the approximate Reynolds stresses from the RANS solver with transpiration cooling. Of specific interest is the off-diagonal $\overline{u'v'}$ component of the Reynolds stress which contributes to the momentum transfer in the boundary layer. The Reynolds stresses can be estimated by recalling the Boussinesq eddy-viscosity hypothesis:

$$\overline{u_i' u_j'} = \frac{2}{3} k \delta_{ij} - \nu_t \left(\frac{\partial \overline{u_i}}{\partial \overline{x_j}} + \frac{\partial \overline{u_j}}{\partial \overline{x_i}} \right) \tag{5.2}$$

For $i = 1$ and $j = 2$, we can estimate the $\overline{u'v'}$ term. The Reynolds stresses from the DNS are temporally-averaged over at least 15 snapshots and along the span. The duration of the temporal averaging varied depending on availability of the stored data from Christopher et al. [37]. Despite this, we do note slight fluctuations in the turbulence statistics of the DNS (especially downstream of the transpiration zone) which may be attributable to a lack of statistical convergence of the Reynolds stresses in the DNS database. For the uniform blowing case the $\overline{u'v'}$ term is compared at the start ($x/\delta_i = 30$), at about the middle, ($x/\delta_i = 36$), and slightly downstream of the transpiration zone ($x/\delta_i = 52$) in Figure 5.12. At the start of the transpiration region, the Reynolds stress profiles for all

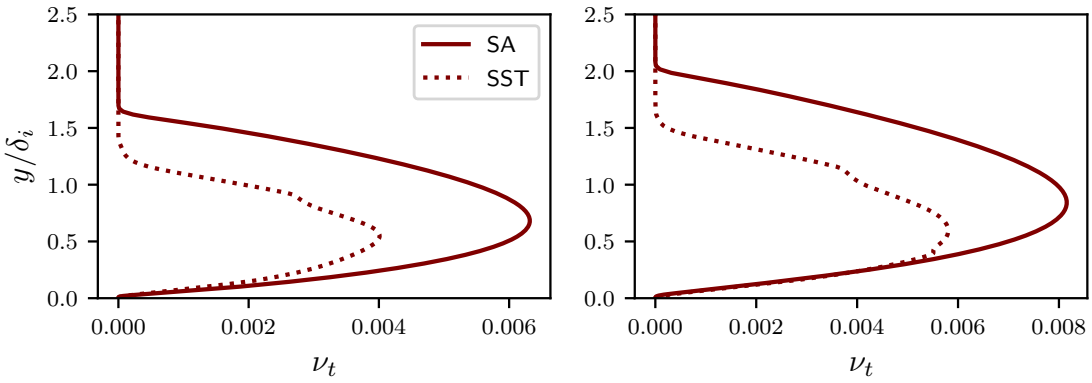

Figure 5.11 Eddy viscosity at the middle ($x = 41\delta_i$, left) and downstream of the transpiration zone ($x = 59\delta_i$, right) for $F = 0.6\%$.

blowing ratios collapse, as expected, for the all the RANS and DNS results. Over the transpiration region ($x/\delta_i = 36$), the $\overline{u'v'}$ term increases monotonically with the blowing ratio. Although the RANS computations over-predict the Reynolds stresses, the location of the peaks is consistent between the RANS and DNS. The compounded over-prediction of turbulence becomes evident after the transpiration region, especially for the high blowing ratio. Although we note a good match in the wall normal location of the peak.

For the slits blowing case, there is a repeating sequence of transpired fluid followed by a sudden reattachment of the flow to the cooled wall. Figure 5.13 shows the Reynolds stresses at the center of a wall and transpiration slit at about the middle of the transpiration zone. Over both the wall and transpiration regions, the turbulent stresses are drastically over-predicted by the RANS. This corroborates the previous observation that the boundary layer height was over-predicted over the transpiration region in the slit case.

The turbulent heat flux plays a critical role in thermal mixing of a turbulent boundary layer with transpiration. The turbulence-driven heat fluxes are modeled using the gradient diffusion hypothesis which relates, $\overline{v'T'}$, to the temperature gradient in the wall normal direction:

$$-\rho\overline{v'T'} = \frac{\mu_t}{Pr_t}\frac{\partial T}{\partial y} \tag{5.3}$$

The proportionality constant between the turbulent flux and mean flow gradients is tied to

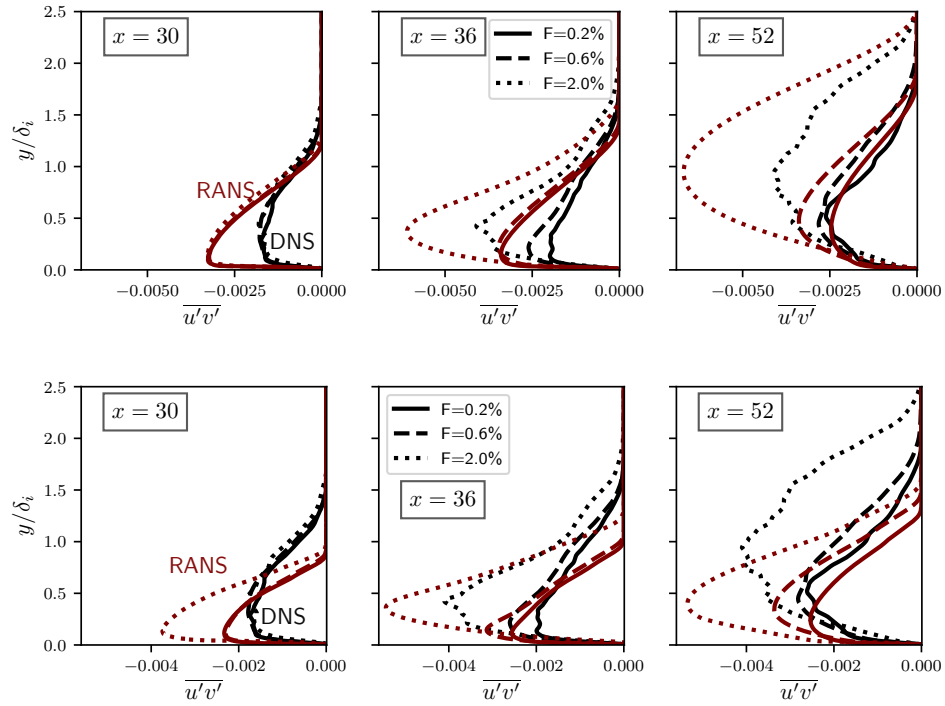

Figure 5.12 Reynolds stress comparison in the uniform transpiration case. The SA (top row) and SST (bottom row) model are compared against the DNS.

the ratio of turbulent viscosity and turbulent Prandtl number, Pr_t. In addition to this rather primitive modeling assumption, the Pr_t has a significant impact on the thermal distribution, this has been confirmed in film cooling [78]–although the effects are expected to be similar in transpiration cooling. Many works have considered more advanced modeling, see e.g. [79, 80], to account for the variable Pr_t which may be physically observed. In the present work, in absence of a justifiable value for Pr_t, we simply set it to unity. As noted in the temperature distribution, the RANS turbulent heat flux match surprisingly well with the DNS in the uniform case (Figure 5.14, left), although we notice an under-prediction in the outer boundary layer. The lower $\overline{v'T'}$ in the outer boundary results in a under-prediction in the thermal boundary layer thickness as shown in Figure 5.4. For the slits cases in Figure 5.14 (middle and right), we note a clear over-prediction of the turbulent heat flux, which thickens the thermal boundary layer (Figure 5.5). A case-specific or a variable turbulent Prandtl number may be required to adequately match the momentum and thermal

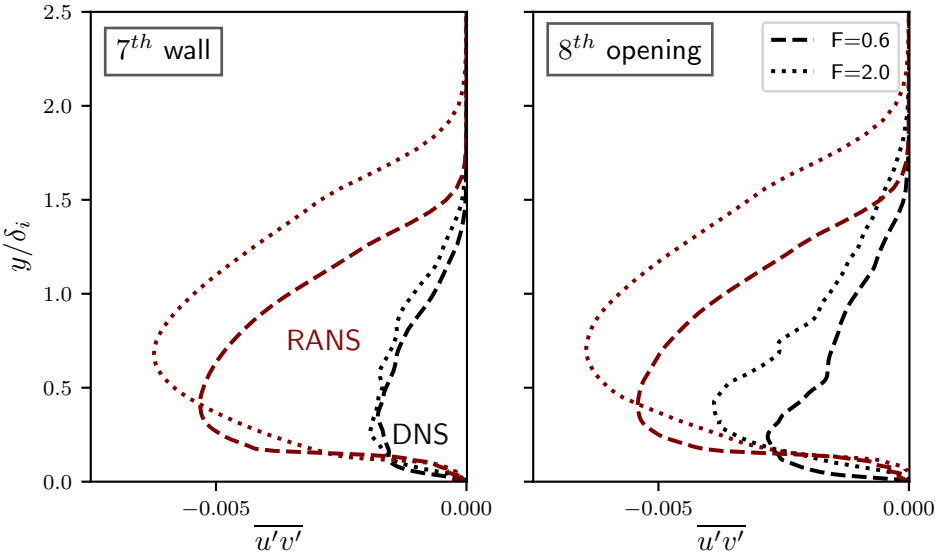

Figure 5.13 Reynolds stress comparison in the slits transpiration case using the SA model. We evaluate the profile at the center of the 7^{th} wall segment (left) and 8^{th} transpiration segment (right).

distributions but these considerations fall outside of the scope of the current work.

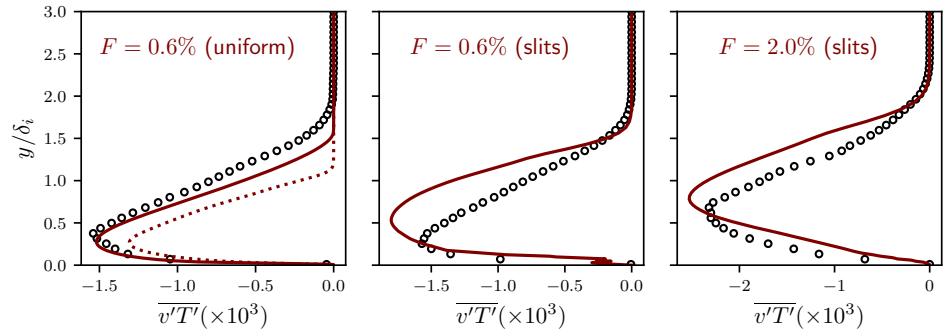

Figure 5.14 Turbulent heat transfer, $\overline{v'T'}$ at $x = 41\delta_i$ using the SA model (full line). On the left pane, the SST model is shown as a dashed line. The symbols correspond to the spatio-temporally-averaged DNS results.

5.2 High-speed Shock Vector Control simulations

The following section will discuss the information needed to assess the applicability of transpiration cooling as a means for Shock Vector Control (SVC).

5.2.1 Parametric study of important variables

For current SVC systems to operate efficiently, the shock angle and location must be controlled to eliminate shock reflection on the opposite wall. Similarly, if transpiration cooling is to be used as a substitute to current configurations, an understanding of the blowing ratio and the resultant shock wave formation must be sought. For a freestream inlet of Mach 6, several blowing ratios were tested. The resultant shock wave angle, location relative to the start of transpiration, non-dimensional force and moment on the plate can be seen in Table 5.1. The force and moment are non-dimensionalized by dividing by the force and moment of the baseline case ($F = 0.874$). The moment is measured about the start of the plate at $x = 0$. The separation location and the force on the plate have a linear relationship with the blowing ratio. While the shock angle and moment on the plate are best approximated by a polynomial relationship. The plate force is linear because as the blowing ratio increases, the pressure at the plate increases linearly. Whereas, when the blowing ratio

F	θ[deg]	x[m]	Force($\frac{F_{plate}}{F_0}$)	Moment($\frac{M_{plate}}{M_0}$)
0	10.831	0.000	0.908	0.879
0.444	12.557	-0.015	0.931	0.925
0.874	13.465	-0.036	1	1
1	13.679	-0.041	1.015	1.0144
1.5	14.154	-0.058	1.078	1.068
2	14.423	-0.074	1.149	1.123

Table 5.1 Shock angle and location in front of transpiration vs F

increases the area over which the higher post shock pressure acts increases negligibly. A linear increase in pressure and a negligible increase in area result in a linear increase in force. However, the marginal increase in the area of the post-shock region does not have a linear relationship with the resultant moment. This is a direct result of the definition of a moment. As the separation location moves farther away from the center of rotation, a constant force would exert a larger moment. However, with increasing distance the force post-shock is increasing linearly, as stated before. This leads to the moment being well approximated by a 2^{nd}-order polynomial.

Another important characteristic of hypersonic flow is the Mach line that separates the subsonic flow, near the wall, and the supersonic flow above. Information below the Mach line, such as pressure waves, can propagate upstream. This also means that there are no shocks below the Mach line. The effect of blowing ratio on the Mach line can be seen in Figure 5.15. Critical information can be obtained from the Mach line diagram. The start of the separation shock is well approximated by a sudden change in the slope on the Mach line, before the transpiration region. The upstream portion represents a normal boundary layer development, followed by a sudden increase in slope due to an increase in temperature post shock (increasing the speed for Mach 1), and larger boundary layer growth, slowing velocity close to the wall. The peak height of the Mach curve also corresponds to a higher pressure at the plate.

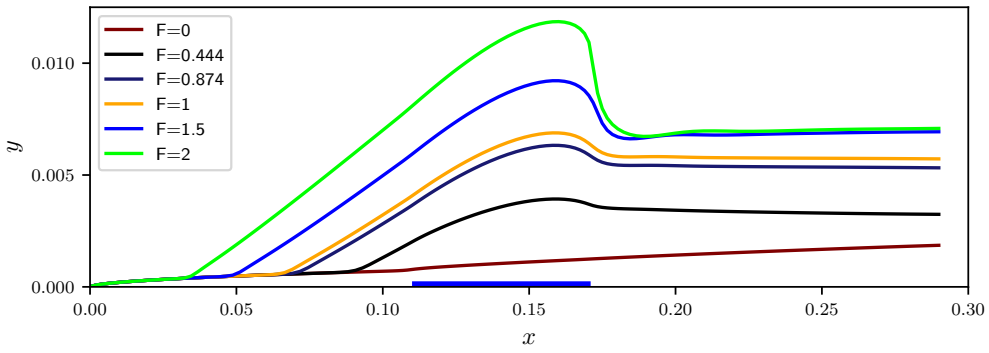

Figure 5.15 Effect of blowing ratio on the Mach line.

Mach	F	θ[deg]	x[m]	Force($\frac{F_{plate}}{F_0}$)	Moment($\frac{M_{plate}}{M_0}$)
5	0.955	15.381	-0.039	0.963	0.957
6	0.874	13.465	-0.036	1	1
7	0.820	12.141	-0.035	1.044	1.050

Table 5.2 Effect of freestream Mach number on the flow.

The freestream Mach number is a defining condition for any flow. The effect of keeping the transpiration velocity constant and changing the freestream Mach number was investigated, and the important values summarized in Table 5.2. For the same transpiration flow speeds, the calculated blowing ratio increases inversely to the freestream Mach number (based on the definition of F). This relationship is a result of superimposing a few key factors. Firstly, as the freestream Mach number is increased, the denominator of the blowing ratio increases. However, as the Mach number is increased, the post shock pressure on the plate also increases, resulting in larger density of the transpired fluid. The effect of the increase in denominator is larger than the increase of the numerator, so the overall blowing ratio decreases. The Mach lines for the varying inlet Mach number can be seen in Figure 5.16. It should be noted that lower inlet Mach numbers produce a higher peak in the Mach line. However, this is the only case where a higher peak in the Mach line does not generate a higher pressure on the plate. This can be understood by examining the boundary layer growth of a laminar flow and the momentum balance. A typical laminar boundary layer

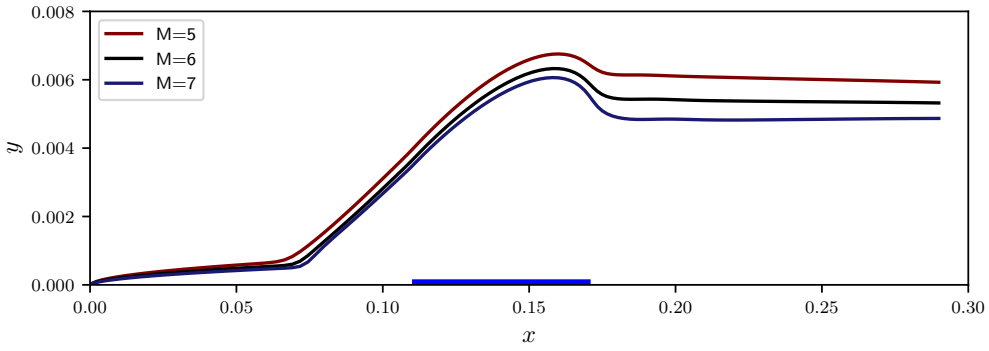

Figure 5.16 Effect of Mach number on Mach line.

grows according to the Blasius solution, where the boundary layer thickness is given by equation (5.4):

$$\delta_{99}(x) \approx 5.0\sqrt{\frac{\nu x}{u_0}} \tag{5.4}$$

Naturally, as the flow speed is decreased, the boundary layer and Mach line will increase in height. Additionally, from a momentum perspective, a decrease from Mach 6 to Mach 5 represents a 17% decrease in incoming momentum (assuming the same inlet temperature). While, due to compressibility, the transpired momentum decreases by only 10%. This allows the slower transpired fluid to flow higher into incoming flow and raise the Mach line, without increasing the pressure.

Next, the entrance length before transpiration will be examined to understand the impact of transpiration location (and boundary layer height) on the performance. In addition to the standard $F = 0.874$ case with an entrance length of 0.11 meters, 2 additional cases, half and double the entrance length, will be compared using the same transpiration velocity. The cases are summarized in Table 5.3. The shorter the entrance length, the smaller the displaced momentum thickness giving rise to a larger blowing ratio. An interesting note for this configuration is the shock location in front of the transpiration region increases with blowing ratio breaking trends from the previous comparisons, while all other trends still hold (angle, force and moment).

For a better visual perspective, the Mach lines are plotted with $x = 0$ being the start of

l_{ent}	F	θ [deg]	x [m]	Force ($\frac{F_{plate}}{F_0}$)	Moment ($\frac{M_{plate}}{M_0}$)
0.055	0.961	14.491	-0.0214	1.592	0.937
0.11	0.874	13.465	-0.036	1	1
0.22	0.798	12.249	-0.0567	0.881	1.855

Table 5.3 Effect entrance length evolution on the flow.

transpiration in Figure 5.17.

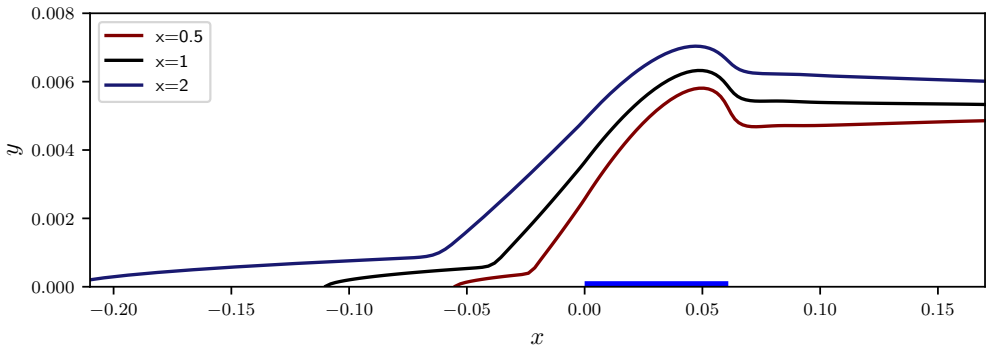

Figure 5.17 Effect of entrance length on Mach line.

This section demonstrated that the overall characteristics of the flow could be controlled by influencing the blowing ratio, speed of the external flow and position of the transpiration region. These results show evidence of the controllability of the shock structures in transpiration cooling that can be leveraged for SVC.

5.2.2 Effect of turbulence on flow

In Chapter 4, the experimental setup of Gülhan and Braun [9] was replicated. The flow was described as laminar due to the freestream conditions. The laminar case slightly overpredicted the boundary layer growth, which subsequently resulted in a larger angle for the separation shock for a plate at -5 degrees. After examining the small effect of the entrance length on the shock characteristics, a turbulent RANS simulation was attempted to

see if the Reynolds stresses have a big impact in the post shock region. The reader should bear in mind that the upstream turbulence can greatly effect the shock characteristics [81].

When changing the flow characteristic to turbulent, the upstream flow pre-shock is not affected as the turbulent kinetic energy is very low. After the shock, the momentum profile of the flat plate at -5 degrees showed closure alignment to the experimental results, as seen in the Schlieren image of the turbulent case, Figure 5.18, when compared to the laminar case in Figure 4.4. When comparing Figures 4.4 and 5.18, it is clear that the turbulent

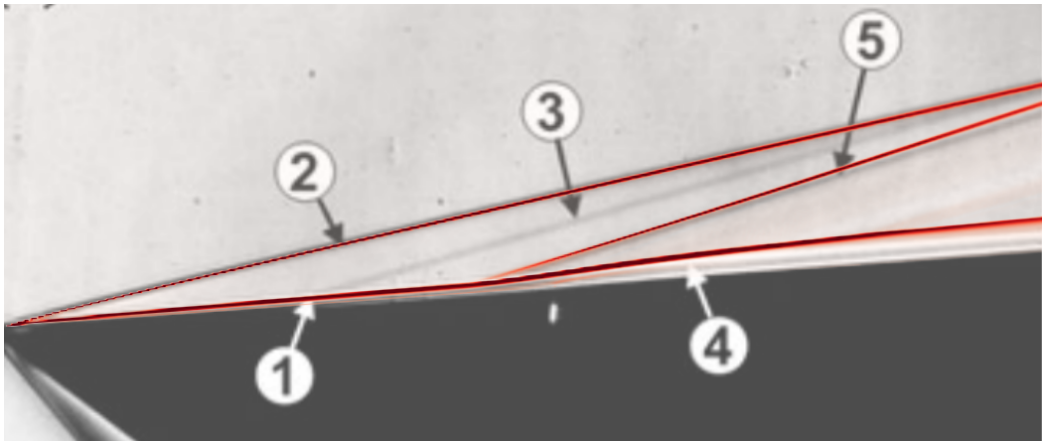

Figure 5.18 Effect of turbulence on -5 degree plate.

model captures the boundary layer height and shock angle more precisely. However, there is a limitation when trying to reproduce the work of Gülhan and Braun [9]. When the original model was constructed, the post shock temperature boundary condition was set to an average heat flux that would capture the gradual increase of temperature within the error of the colour map, as seen in Figure 4.6. Attempting to replicate this method was not possible for the turbulent case. For a low heat flux into the plate, the start of the downstream plate would match the experimental results. However, further down stream the temperature would rise several hundred Kelvin above the experimental results. Attempting to compensate by raising the heat flux into the wall would result in a temperature at the start of the downstream plate, which was lower than the temperature of the transpired fluid resulting in a non-physical solution. To model the experimental results properly, a variable heat flux approach would have to be undertaken but the exact values remain unknown.

However, the goal of this research is not to replicate results but instead develop an understanding of the flow. As such, the focus will shift to comparing two identical cases with the only difference being the addition a $k-\omega$ SST model and comparing and contrasting the results. The turbulent case will build upon case 3 in Table 3.3, with no angle of attack. The number of mesh elements was increased to 2669×654 (x-y), to achieve a $y+ \approx 1$ and keep the aspect ratio below 100. The results of this study are summarized in Table 5.4. Additionally, the sonic line can be seen in Figure 5.19. The rapid decrease in the Mach

Type	F	θ[deg]	x [m]	Force ($\frac{F_{plate}}{F_0}$)	Moment ($\frac{M_{plate}}{M_0}$)
laminar	0.874	13.465	-0.036	1	1
turbulent	0.829	13.118	-0.028	1.009	1.003

Table 5.4 Impact of turbulence on the flow.

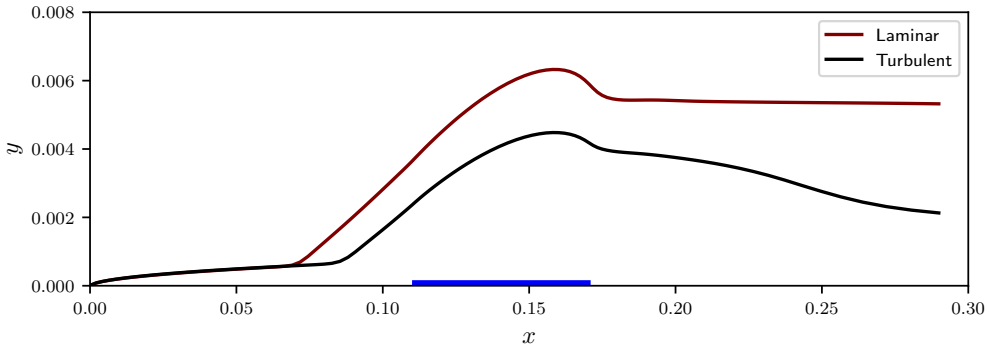

Figure 5.19 Effect of turbulence on Mach line.

line post transpiration is an interesting result, which requires further investigation. The development of a boundary layer is approximated by the Blasius solution given by equation (5.4) and the turbulent case is given by equation (5.5).

$$\delta_{99}(x) \approx 0.37 \frac{x}{Re_x^{\frac{1}{5}}} \tag{5.5}$$

Theoretically, this implies that the boundary layer height, defined by δ_{99}, should be higher than the laminar case and one would incorrectly assume that the Mach line would also be

higher. However, the gradient, $\frac{du}{dy}$, at the wall is much larger in the turbulent case, resulting in faster velocity near the wall. Figure 5.20 shows the boundary layer near the wall for both laminar and turbulent cases at $x = 0.25$. The velocity at Mach 1 is overlaid as well, and the intersection between the case velocity and Mach line is the resultant height of the Mach line at that location. The velocity at Mach 1 is calculated using equation (5.6).

$$V_{M=1} = \sqrt{\gamma RT} \tag{5.6}$$

As seen in figure 5.20, the velocity gradient at the wall is much steeper in the turbulent case,

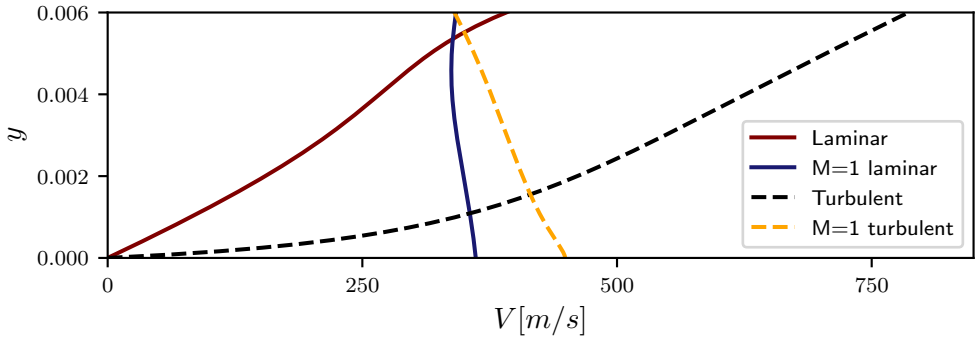

Figure 5.20 Near wall velocity profile and local speed of sound (denoted $M = 1$) at $x = 0.25$.

as expected. Due to higher thermal heating for the turbulent case, the temperature is higher near the wall and the speed of sound is also higher. Had enough heat been removed from the downstream plate to match the thermal profile of the laminar case, the speed of sound would be further depressed. This understanding is especially useful for cases that involve multiple transpiration regions or a combination of injectors and a transpiration region, similar to the works of Anderson et al. [55] and Waithe and Deere [56]. Having the ability to control the Mach line height for the preceding transpiration zone can aid in controlling the forces and moments on the plate as shown in the previous section.

5.2.3 Can shock vector control and transpiration cooling be used synergetically?

To answer this question, it must first be shown that a similar separation distance can be achieved with transpiration cooling as is typically shown for classical SVC injection technique with a comparable blowing ratio. Next, a suitable location must be determined, that requires both high cooling (using transpiration) and a high potential for actuation (using SVC).

As discussed in Chapter 2, blunt-body dynamic model was developed as a model for SVC by contributions from Zukoski and Spaid [4], Spaid [47], Zukoski [48], and Maarouf [12]. Blunt body dynamic model was developed as a low order model to analytically describe SVC by means of injectant fluid. Younes and Hickey [11] investigated the sensitivity of the model, validated against several works, [3, 7, 12, 54, 56–58, 82, 83] a maximum sensitivity of 13% was noted. Figure 5.21 is the schematic for the implemented nozzle. From this code,

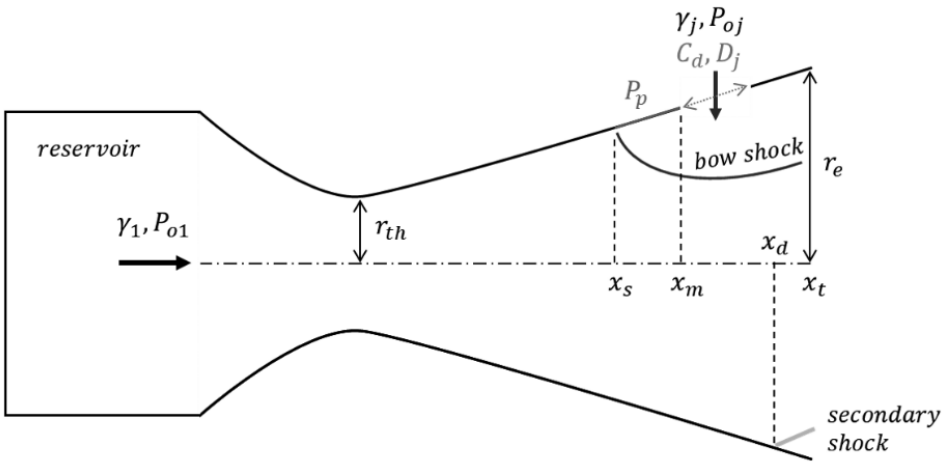

Figure 5.21 Schematic diagram of model domain employed by Younes and Hickey [11]

the module that calculated penetration height h and separation location, x_s, was adapted to the flat plate hypersonic SVC for the cases in Table 5.1, excluding the zero blowing ratio case. Blunt body dynamics will be used to generate a prediction for injection height and separation distance. This in turn, will be compared to the simulation work to determine if a simple analytical model can be used as a 1^{st} order approximation. Equation (5.7) gives the

penetration height, h, for the blunt body dynamics model as developed my Maarouf [12]:

$$h = \frac{2C_d b P_{0j} \gamma_j}{p_0 - p_{av} + \frac{1}{3} p_0 \gamma_0 M_0^2 C_{Pmax}} \left(\frac{2}{\gamma_j + 1}\right)^{\frac{1}{\gamma_j - 1}} \left[\frac{1}{\gamma_j^2 - 1}\left(1 - \left(\frac{p_j}{P_{0j}}\right)^{\frac{\gamma_j - 1}{\gamma_j}}\right)\right]^{\frac{1}{2}} \tag{5.7}$$

Here C_d is the discharge coefficient and is set to 1, b is the width of the opening and $\gamma = 1.4$ The subscript $_0$ corresponds to stagnation values, $_j$ for injectant values and $_{av}$ to after separation shock properties. C_P is defined as $\frac{p - P_0}{q_0}$ and specifically C_{Pmax} is where p is maximum on the blunt-body. For more info on calculating C_{Pmax}, the reader is directed to the thesis of Maarouf [12]. The penetration height is compared to the maximum height of the Mach line in Figure 5.22. There is very good agreement between analytical and simulated results around a blowing ratio of unity. The penetration height in the blunt body

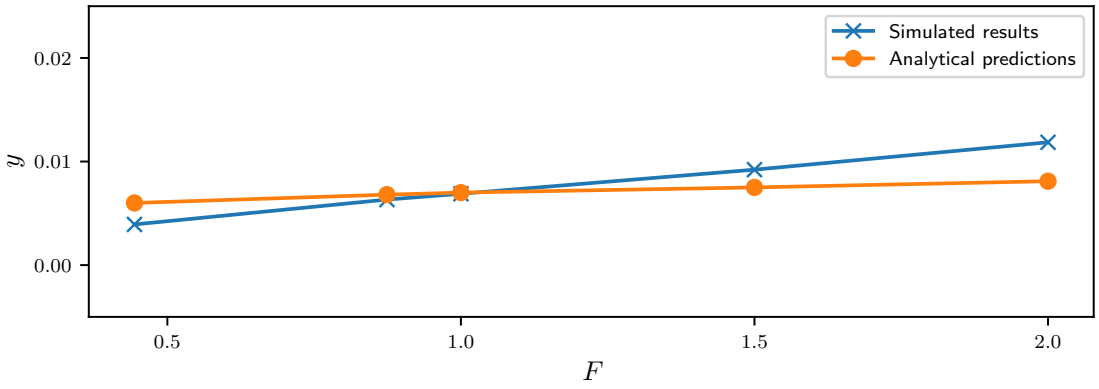

Figure 5.22 Analytical penetration height, h, versus the peak height of the Mach line for various blowing ratios

model is directly correlated to the separation distance using the geometric relationships in (5.8) to solve for β and (5.9) to solve for ϵ. The geometry describing the variables in the preceding equation is shown in Figure 5.23.

$$\frac{P_p}{P_{s(x)}} = \frac{2\gamma * M_{s(x)}^2 \sin^2\beta - (\gamma - 1)}{\gamma + 1} \tag{5.8}$$

$$\tan\epsilon = \frac{M_{s(x)}^2 \sin^2\beta - 2\cot\beta}{2 + M_{s(x)}^2(\gamma + \cos 2\beta)} \tag{5.9}$$

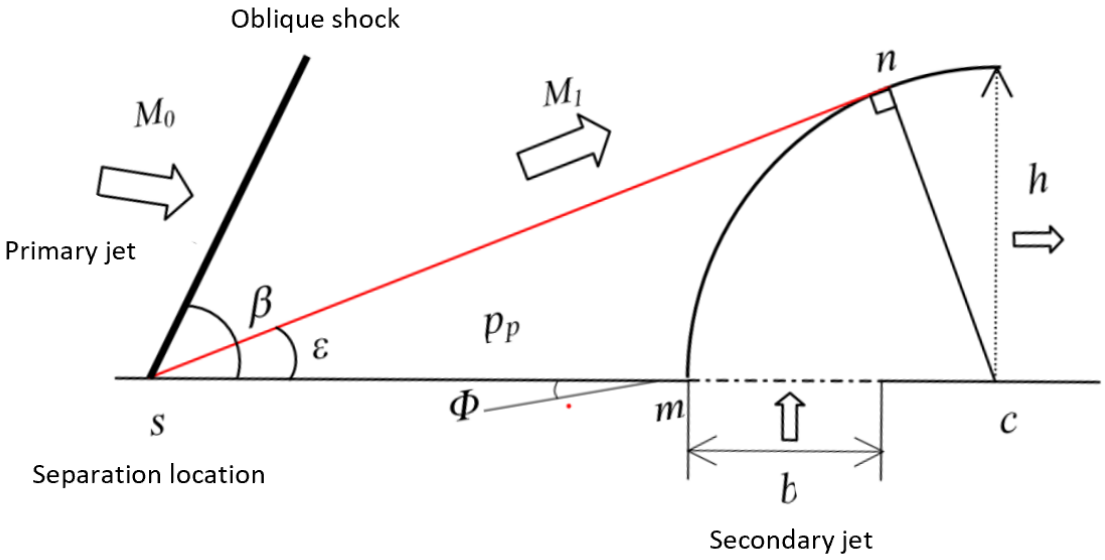

Figure 5.23 Geometric representation of equations 5.8 and 5.9, adapted from Maarouf [12].

Solving the aforementioned equations yields the results in Figure 5.24, where the analytical model is compared to the results of the simulations. Below a blowing ratio of 1, these models show relatively good agreement and could be used as a first order approximation. In previous sections it was shown that with increasing blowing ratio, the peak of the Mach

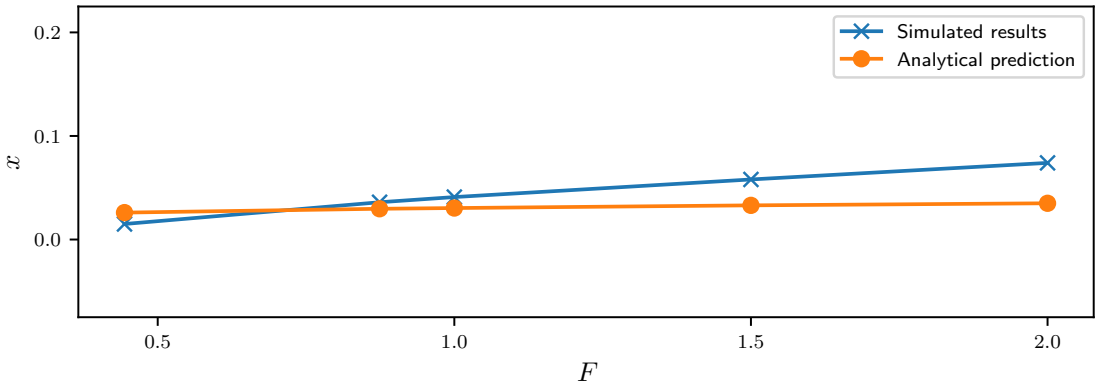

Figure 5.24 Separation distance as predicted by the blunt-body model versus the simulations

line would be pushed upwards and away from the plate. The flow below the line can't

experience a shock wave due to its subsonic nature. This exercise shows an analogue between the penetration distance in blunt body dynamics, and the peak Mach line location in a transpiration flow. It also demonstrates that for the initial design phase, the blunt-body model may be a staring location to determine the possible integration of transpiration cooling and SVC.

To understand the need for transpirative cooling technology, Figure 5.25 demonstrates a typical over-expanded nozzle temperature profile as simulated and validated by Shariatzadeh et al. Shariatzadeh et al. [13]. Typical nozzle locations that would benefit from transpiration

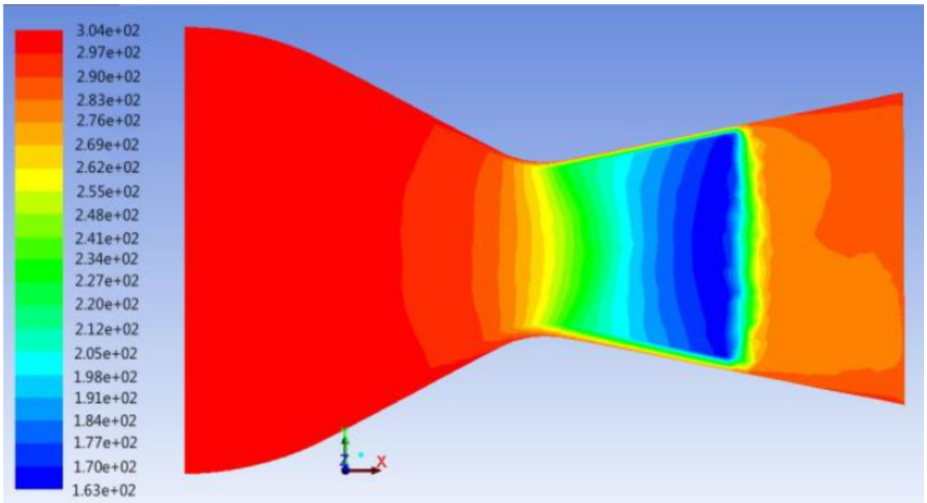

Figure 5.25 Schematic of typical over-expanded nozzle temperature distribution [13]

cooling would be the throat in at all design conditions: over-expanded and under-expanded. As well, the walls near the exit in the over-expanded scenario, due to high back pressure, would also benefit form transpiration cooling. Using the model by Younes and Hickey [11], two configurations of injection cooling were tested to determine the effectiveness of SVC at each location. A configuration similar to Figure 5.21, with the start of injection near the exit of the nozzle was tested, followed by a case where the nozzle was moved towards the throat. As this is a Laval nozzle, the Mach number is not constant through out. As has been shown in the previous sections, a change in Mach number will have an impact on the forces, moments, Mach line and overall blowing ratio for a cross flowing constant velocity injectant. The specifications for the Laval nozzle with an 8.5 deg angled circular injection

port is examined, the nozzle characteristics, with no injection, are outlined in Table 5.5.

The resultant forces and deflection angle of the studied over-expanded cases can be seen in Table 5.6 for two different injection locations, $\frac{x_m}{x_t}$.

NPR	SPR	γ	M_{exit}	$\frac{A_{exit}}{A^*}$
30.7	1	1.4	2.88	3.777

Table 5.5 Analytical model conditions

$\frac{x_m}{x_t}$	F_x	F_y	δ
0.7	1174	99	4.8
0.9	1171.0	80	3.9

Table 5.6 Analytical model results

The lowest value of $\frac{x_m}{x_t}$ without the shock reflecting off the opposite side of the nozzle is 0.7. This is important as the model Younes and Hickey [11] cannot handle a reflecting shock wave. The force in the cross flow direction increases monotonically as the injection fluid is moved farther toward the throat, until a reflecting shock appears. At this point, pressure is increased on both sides of the nozzle, decreasing the ability to deflect the thrust.

A single stage rocket may be an ideal candidate to attempt transpiration cooling and SVC. Specifically a location near the exit of the nozzle, as it would be easier to model without reflecting shocks. The design condition for a Laval nozzles is to have a back pressure that is lower than atmospheric. At launch, the back pressure would be higher than the design condition, resulting in higher temperature profiles similar to Figure 5.25. At lower altitudes, it is not as important to vector thrust and transpiration cooling can operate without significant thrust vectoring. As the rocket ascends, the shock wave would move towards the exit of the nozzle until an under-expand configuration is reached, at which point transpiration cooling would likely not be required. However, farther away from the Earth's surface, more SVC would be required. In this case, certain sections of the transpiration cooling apparatus could be left on to deflect thrust as needed.

Chapter 6

Conclusion

This work seeks to advance the understanding of RANS-based predictive modeling for transpiration cooling while providing a proof-of-concept for the application of transpiration cooling for shock thrust vector control (SVC). This work is divided in two distinct but necessary parts. First, we study a transpiratively-cooled turbulent compressible boundary layer flow over a strongly cooled flat plate and, second, a hypersonic flow over a flat plate where SVC is analysed in tandem with transpiration.

To this end, we conduct a comparative study of a high-fidelity DNS database and analogous RANS simulations on a fully turbulent boundary layer with cooled walls and transpiration cooling at low Mach number ($M = 0.3$). Two types of transpiration cooling setups are investigated: uniform and slit blowing. The DNS and RANS cases were designed to have nearly identical flow characteristics with slight differences in the inlet boundary condition. We match the boundary layer characteristics upstream of the transpiration region between the RANS and DNS which enables a direct comparison of the simulations. Notably, having complete access to the turbulent stresses in the DNS, we can assess the RANS models under these challenging conditions.

Overall, RANS models capture the salient features of transpiration cooling at all blowing ratios. As noted by other works, the RANS models over-predict the wall turbulence which results in an increase in the momentum transfer in the boundary layer and, consequently,

a thicker boundary layer compared to the DNS for the uniform blowing case. Yet, this increased turbulence production does not translate into an over-prediction in the temperature distribution. The thermal mixing is incorrectly captured which invites a deeper consideration of either the turbulent thermal flux modeling or a modification to the turbulent Prandtl number. When modeling the slit case, an even greater turbulence production relative to the comparative DNS is noted. As this case is characterized by 14 individual blowing slits, there is an over-production of turbulence at the start of each blowing slit. This compounding effect results in a thicker thermal (and momentum) boundary layer and smaller thermal gradient at the wall compared to the DNS.

Furthermore, the scope of analysis was expanded to consider the applicability of RANS model to high-speed flows. To this end, we validated our results against available experimental data at hypersonic speed ($M = 6$). The laminar case was built up by replicating the experimental case at a -5 angle-of-attack (AOA) and matching the plate temperature profile, as well as resultant shock wave formation. After case was validated, the AOA was set to 0, and parameters such as blowing ratio, inlet Mach number, entrance length and turbulence were varied to understand their effect on the flow and resulting shock.

It was found that as the blowing ratio is increased, the resultant shock angle, separation distance force and, moment on the plate all increase. However, this increase is not linear in all cases. Additionally, with increasing blowing ratio, the Mach line is pushed farther upward into the flow, which is the cause of the higher shock angle. Varying the inlet Mach number showed similar results when organized as mentioned above. When compared to blowing ratio, however, the force and moment were increased with decreasing blowing ratio. The effect of boundary layer thickness on flow characteristics is demonstrated by varying the entrance length of the flow. When compared to the resultant blowing ratio, the separation distance and moment on the plate increased with decreasing blowing ratio. The final parameter to be varied was turbulence. This caused forces and moments to increase slightly, while the shock angle and separation distance decreased.

Lastly, the results were compared to blunt body dynamics to predict the separation distance for a typical Laval nozzle. Agreement was found at low blowing ratios, leading to

the conclusion the transpiration cooling may be a suitable option for thrust vector control used for single stage rockets.

References

[1] S. Hillcoat, J.-P. Hickey, Pressure fluctuations under a turbulent boundary layer with transpiration cooling, in: AIAA AVIATION 2021 FORUM, 2021, p. 1. URL: https://arc.aiaa.org/doi/abs/10.2514/6.2021-2605. doi:10.2514/6.2021-2605. arXiv:https://arc.aiaa.org/doi/pdf/10.2514/6.2021-2605.

[2] W. A. McConarty, F. M. Anthony, Design and evaluation of active cooling systems for Mach 6 cruise vehicle wings, Technical Report December, 1971.

[3] M. Sellam, V. Zmijanovic, L. Leger, A. Chpoun, Assessment of gas thermodynamic characteristics on fluidic thrust vectoring performance: Analytical, experimental and numerical study, International Journal of Heat and Fluid Flow 53 (2015) 156–166. URL: http://dx.doi.org/10.1016/j.ijheatfluidflow.2015.03.005https://pdf.sciencedirectassets.com/271482/1-s2.0-S0142727X15X00026/1-s2.0-S0142727X15000272/main.pdf?X-Amz-Security-Token=IQoJb3JpZ2luX2VjEI%2F%2F%2F%2F%2F%2F%2F%2F%2F%2FwEaCXVzLWVhc3QtMSJGMEQCIA. doi:10.1016/j.ijheatfluidflow.2015.03.005.

[4] E. E. Zukoski, F. W. Spaid, Secondary injection of gases into a supersonic flow, AIAA Journal 2 (1964) 1689–1696. URL: https://authors.library.caltech.edu/21600/1/162_Zukoski_EE_1964.pdf. doi:10.2514/3.2653.

[5] R. E. Walker, M. Shandor, Influence of injectant properties for fluid-injection thrust vector control, Journal of Spacecraft and Rockets 1 (1964) 409–413. doi:10.2514/3.27670.

[6] J. G. Santiago, J. C. Dutton, Velocity measurements of a jet injected into a supersonic crossflow, Journal of Propulsion and Power 13 (1997) 264–273. doi:10.2514/2.5158.

[7] V. Zmijanovic, V. Lago, M. Sellam, A. Chpoun, Thrust shock vector control of an axisymmetric conical supersonic nozzle via secondary transverse gas injection, Shock Waves 24 (2014) 97–

111. doi:10.1007/s00193-013-0479-y.

[8] A. Kurganov, E. Tadmor, New High-Resolution Central Schemes for Nonlinear Conservation Laws and Convection-Diffusion Equations, Journal of Computational Physics 160 (2000) 241–282. doi:10.1006/jcph.2000.6459.

[9] A. Gülhan, S. Braun, An experimental study on the efficiency of transpiration cooling in laminar and turbulent hypersonic flows, Experiments in Fluids 50 (2011) 509–525. doi:10.1007/s00348-010-0945-6.

[10] A. Gülhan, RESPACE - Key Technologies for Reusable Space Systems, 2008. URL: https://link.springer.com/content/pdf/10.1007/s00348-019-2774-6.pdf. doi:I10.1007/978-3-540-77819-6.

[11] K. Younes, J. P. Hickey, Fluidic thrust shock-vectoring control: A sensitivity analysis, AIAA Journal 58 (2020) 1887–1890. doi:10.2514/1.J058922.

[12] N. Maarouf, Modélisation des phénomènes dissymétriques dans le divergent des tuyères supersoniques propulsives: application a la vectorisation de la poussée, Ph.D. thesis, L'UNIVERSITÉ D'ÉVRY-VAL D'ESSONNE, 2008. URL: https://www.biblio.univ-evry.fr/theses/2008/2008EVRY0024.pdf.

[13] O. J. Shariatzadeh, A. Abrishamkar, A. J. Jafari, Computational Modeling of a Typical Supersonic Converging-Diverging Nozzle and Validation by Real Measured Data, Journal of Clean Energy Technologies 3 (2015) 220–225. doi:10.7763/jocet.2015.v3.198.

[14] F. S. Milos, Y.-k. Chen, T. H. Squire, Updated Ablation and Thermal Response Program for Spacecraft Heatshield Analysis, Technical Report, NASA Ames Reserach Center, 2006.

[15] M. A. Keller, M. J. Kloker, Direct numerical simulation of foreign-gas film cooling in supersonic boundary-layer flow, AIAA Journal 55 (2017) 99–111. doi:10.2514/1.J055115.

[16] A. Wagner, M. Kuhn, J. Martinez Schramm, K. Hannemann, Experiments on passive hypersonic boundary layer control using ultrasonically absorptive carbon-carbon material with random microstructure, Experiments in Fluids 54 (2013). doi:10.1007/s00348-013-1606-3.

[17] Y. Zhu, W. Peng, R. Xu, P. Jiang, Review on active thermal protection and its heat transfer for airbreathing hypersonic vehicles, Chinese Journal of Aeronautics 31 (2018) 1929–1953. doi:10.1016/j.cja.2018.06.011.

[18] A. Herbertz, M. Ortelt, I. Müller, H. Hald, c*-Efficiency evaluation of transpiration cooled

ceramic combustion chambers, CEAS Space Journal 6 (2014) 99–105. doi:10.1007/s12567-014-0062-0.

[19] A. V. van Foreest, M. Sippel, J. Klevanski, Transpiration Cooling to Handle the Aerothermodynamic Challenges of the SpaceLiner Concept, Challenges (2007) 1–12.

[20] R. D'Agostino, Elon Musk: Why I'm Building the Starship out of Stainless Steel, Popular Mechanics (2019).

[21] G. Sutton, O. Biblarz, Rocket Propulsion Elements, 2001. doi:10.1201/b19031-24.

[22] F. S. Billig, Propellant utilization system, ???? URL: https://patents.justia.com/patent/5135184.

[23] A. Bukva, N. Christopher, J. P. Hickey, Towards modelling of thermal protection systems with transpiration cooling, 23rd AIAA International Space Planes and Hypersonic Systems and Technologies Conference, 2020 (2020). doi:10.2514/6.2020-2456.

[24] A. Bukva, K. Zhang, N. Christopher, J.-P. Hickey, Assessment of turbulence modeling for massively-cooled turbulent boundary layer flows with transpiration cooling, Physics of Fluids 33 (2021) 095114.

[25] M. A. Keller, M. J. Kloker, H. Olivier, Influence of cooling-gas properties on film-cooling effectiveness in supersonic flow, Journal of Spacecraft and Rockets 52 (2015) 1443–1455. doi:10.2514/1.A33203.

[26] A. Cerminara, R. Deiterding, N. Sandham, A mesoscopic modelling approach for direct numerical simulations of transition to turbulence in hypersonic flow with transpiration cooling, International Journal of Heat and Fluid Flow 86 (2020) 108732. URL: https://doi.org/10.1016/j.ijheatfluidflow.2020.108732. doi:10.1016/j.ijheatfluidflow.2020.108732.

[27] N. Christopher, J. M. Peter, M. J. Kloker, J. P. Hickey, DNS of turbulent flat-plate flow with transpiration cooling, International Journal of Heat and Mass Transfer 157 (2020) 119972. URL: https://doi.org/10.1016/j.ijheatmasstransfer.2020.119972. doi:10.1016/j.ijheatmasstransfer.2020.119972.

[28] R. Hink, V. Hannemann, T. Eggers, Extension of the Spalart-Allmaras One-Equation Turbulence Model for Effusive Cooled Rocket Chambers (2014).

[29] F. Chedevergne, Y. Marchenay, Transpired turbulent boundary layers: a general strategy for

RANS turbulence models, Journal of Turbulence 5248 (2019). doi:10.1080/14685248.2019.1702198.

[30] W. Dahmen, S. Müller, M. Rom, S. Schweikert, M. Selzer, J. Von Wolfersdorf, Numerical boundary layer investigations of transpiration-cooled turbulent channel flow, International Journal of Heat and Mass Transfer 86 (2015) 90–100. doi:10.1016/j.ijheatmasstransfer.2015.02.075.

[31] H. Julien, W. Kays, R. Moffat, The turbulent boundary on a porous plate: experiemental study of the effects of a favorable pressure gradient, Technical Report, 1969.

[32] P. Andersen, W. Kays, R. Moffat, The turbulent boundary layer on a porous plate: an experimental study of the fluid mechanics for adverse free-stream pressure gradients, report no. HMT-15, Technical Report, 1972.

[33] V. Avsarkisov, M. Oberlack, S. Hoyas, New scaling laws for turbulent Poiseuille flow with wall transpiration, Journal of Fluid Mechanics 746 (2014) 99–122. doi:10.1017/jfm.2014.98.

[34] S. Kraheberger, S. Hoyas, M. Oberlack, DNS of a turbulent Couette flow at constant wall transpiration up to $Re_\tau = 1000$, Journal of Fluid Mechanics 835 (2017) 421–443. doi:10.1017/jfm.2017.757.

[35] A. Cerminara, R. Deiterding, N. Sandham, Parallel multiscale simulation of hypersonic flow with porous wall injection, The Sixth International Conference on Parallel, Distributed, GPU and Cloud Computing for Engineering 112 (2019). doi:10.4203/ccp.112.11.

[36] A. Cerminara, R. Deiterding, N. D. Sandham, Direct numerical simulation of hypersonic flow through regular and irregular porous surfaces, Proceedings of the 6th European Conference on Computational Mechanics: Solids, Structures and Coupled Problems, ECCM 2018 and 7th European Conference on Computational Fluid Dynamics, ECFD 2018 (2020) 660–671.

[37] N. Christopher, Numerical Analysis of Turbulent Boundary Layer on a Flat Plate, Master's Thesis (2020) 76.

[38] D. Prokein, J. von Wolfersdorf, H. Böhrk, Analysis of anisotropy effects for transpiration cooled CMC leading edges using OpenFOAM, 20th AIAA International Space Planes and Hypersonic Systems and Technologies Conference, 2015 (2015). doi:10.2514/6.2015-3552.

[39] F. R. Menter, Two-equation eddy-viscosity turbulence models for engineering applications, AIAA Journal 32 (1994) 1598–1605. doi:10.2514/3.12149.

[40] D. C. Wilcox, Formulation of the k-ω turbulence model revisited, AIAA Journal 46 (2008) 2823–2838. doi:10.2514/1.36541.

[41] P. S. Andersen, W. M. Kays, R. J. Moffat, Experimental results for the transpired turbulent boundary layer in an adverse pressure gradient, Journal of Fluid Mechanics 69 (1975) 353–375. doi:10.1017/S0022112075001474.

[42] J. Bellettre, F. Bataille, A. Lallemand, A new approach for the study of turbulent boundary layers with blowing, International Journal of Heat and Mass Transfer 42 (1999) 2905–2920. doi:10.1016/S0017-9310(98)00341-X.

[43] D. J. Munk, M. Selzer, H. Böhrk, S. Schweikert, G. A. Vio, Numerical modeling of transpiration-cooled turbulent channel flow with comparisons to experimental data, Journal of Thermophysics and Heat Transfer 32 (2018) 713–735. doi:10.2514/1.T5266.

[44] D. Prokein, J. Von Wolfersdorf, Numerical Simulation of Turbulent Boundary Layers with Foreign Gas Transpiration using OpenFOAM Thermochromic Liquid Crystal Property Inverstigations, in: 7th european conference for aeronautics and space science, 2017, pp. 1–15. doi:10.13009/EUCASS2017-589.

[45] A. Wagner, J. M. Schramm, K. Hannemann, R. Whitside, J.-p. Hickey, Hypersonic Shock Wave Boundary Layer Interaction Studies on a Flat Plate at Elevated Surface Temperature, in: International Shock Interaction Symposium, 2016, pp. 231–243.

[46] S. I. A. Syed Abid Hussain, J.-P. Hickey, B. Godbolt, E. Farnfield, Error quantification among cfd solvers for high-speed, non-adiabatic, wall-bounded turbulent flows, in: AIAA Scitech2021 Forum, 2021, p. 1842.

[47] F. Spaid, A study of secondary injection of gases into a supersonic flow, Ph.D. thesis, California Institute of Technology, 1964. URL: https://thesis.library.caltech.edu/4336/1/Spaid_f_1964.pdf.

[48] E. E. Zukoski, Turbulent Boundary-Layer Separation in Front of a Forward-Facing Step, AIAA Journal 5 (1967) 1746–1753.

[49] V. Zmijanovic, L. Leger, V. Lago, M. Sellam, A. Chpoun, Effects of the inlet gases thermodynamic properties on a fluidically thrust vectorized supersonic nozzle, 18th AIAA/3AF International Space Planes and Hypersonic Systems and Technologies Conference 2012 (2012) 91020. doi:10.2514/6.2012-5932.

[50] V. Zmijanovic, Secondary injection fluidic thrust vectoring of an axisymmetric supersonic nozzle (2013).

[51] A. Glagolev, A. Zubkov, Y. Panov, Interaction between a supersonic flow and gas issuing from a hole in a plate, Fluid Dynamics 3 (1968) 65–67. URL: http://link.springer.com.proxy.lib.uwaterloo.ca/article/10.1007/s10694-014-0423-4?institute=OCUL.waterloo.

[52] J. E. Broadwell, Analysis of the fluid mechanics of secondary injection for thrust vector control, AIAA Journal 1 (1963) 1067–1075. doi:10.2514/3.1726.

[53] J.-M. WU, R. L. CHAPKIS, A. MAGER, Approximate Analysis of Thrust Vector Control by Fluid Injection, ARS Journal 31 (1961) 1677–1685. doi:10.2514/8.5891.

[54] D. J. Wing, V. J. Giuliano, FLUIDIC THRUST VECTORING OF AN AXISYMMETRIC EXHAUST NOZZLE AT STATIC CONDITIONS, in: ASME Fluids Engineering Division Summer Meeting, Fairfield, NJ, 1997, pp. 1–6.

[55] C. J. Anderson, V. J. Giuliano, D. J. Wing, Investigation of hybrid fluidic/mechanical thrust vectoring for fixed-exit exhaust nozzles, 33rd Joint Propulsion Conference and Exhibit, AIAA Journal (1997). doi:10.2514/6.1997-3148.

[56] K. Waithe, K. Deere, EXPERIMENTAL AND COMPUTATIONAL INVESTIGATION OF MULTIPLE INJECTION PORTS IN A CONVERGENT-DIVERGENT NOZZLE FOR FLUIDIC THRUST VECTORING, in: AIAA Applied Aerodynamics Conference, 2003, pp. 2003–3802. URL: https://ntrs.nasa.gov/api/citations/20030064985/downloads/20030064985.pdf.

[57] R. Deng, F. Kong, H. D. Kim, Numerical simulation of fluidic thrust vectoring in an axisymmetric supersonic nozzle, Journal of Mechanical Science and Technology 28 (2014) 4979–4987. doi:10.1007/s12206-014-1119-x.

[58] L. Li, M. Hirota, K. Ouchi, T. Saito, Evaluation of fluidic thrust vectoring nozzle via thrust pitching angle and thrust pitching moment, Shock Waves 27 (2017) 53–61. doi:10.1007/s00193-016-0637-0.

[59] P. Jiang, Z. Liao, Z. Huang, Y. Xiong, Y. Zhu, Influence of shock waves on supersonic transpiration cooling, International Journal of Heat and Mass Transfer 129 (2019) 965–974. URL: https://doi.org/10.1016/j.ijheatmasstransfer.2018.10.043. doi:10.1016/j.ijheatmasstransfer.2018.10.043.

[60] M. Holden, Experimental Studies of Transpiration Cooling With Interaction in Hypersonic Flow, Technical Report, 1994. URL: https://ntrs.nasa.gov/api/citations/19940030459/downloads/19940030459.pdf. doi:10.1007/BF02529502.

[61] H. G. Weller, G. Tabor, H. Jasak, C. Fureby, A tensorial approach to computational continuum mechanics using object-oriented techniques, Computers in Physics 12 (1998) 620. doi:10.1063/1.168744.

[62] P. Nielsen, Validation of rhoCentralFoam for Engineering Applications of Under-Expanded Impinging Free Jets, Electronic Thesis and Dissertation Repository (2019). URL: https://ir.lib.uwo.ca/etd/6789.

[63] F. White, I. Corfield, Viscous Fluid Flow, McGraw-Hill, 2006.

[64] J. Anderson, Hypersonic and High Temerature Gas Dynamics, second edi ed., 2006.

[65] F. White, Fluid Mechanics, seventh ed ed., 2011.

[66] k-omega Shear Stress Transport (SST), 2017. URL: https://www.openfoam.com/documentation/guides/latest/doc/guide-turbulence-ras-k-omega-sst.html.

[67] NASA, Turbulence Modeling Resource: k-w SST, ???? URL: https://turbmodels.larc.nasa.gov/sst.html.

[68] Spalart-Allmaras, 2017. URL: https://www.openfoam.com/documentation/guides/latest/doc/guide-turbulence-ras-spalart-allmaras.html.

[69] P. Spalart, S. Allmaras, A one-equation turbulence model for aerodynamic flows, Recherche Aerospatiale 1 (1994) 5–21.

[70] NASA, Turbulence Modeling Resource: Spalart-Allmaras, ???? URL: https://turbmodels.larc.nasa.gov/spalart.html.

[71] I. Bermejo-Moreno, J. Bodart, J. Larsson, B. M. Barney, J. W. Nichols, S. Jones, Solving the compressible Navier-Stokes equations on up to 1.97 million cores and 4.1 trillion grid points, International Conference for High Performance Computing, Networking, Storage and Analysis, SC (2013) 1–10. doi:10.1145/2503210.2503265.

[72] J. Jiménez, S. Hoyas, M. P. Simens, Y. Mizuno, Turbulent boundary layers and channels at moderate Reynolds numbers, Journal of Fluid Mechanics 657 (2010) 335–360. doi:10.1017/S0022112010001370.

[73] E. Luthman, N. Cymbalist, D. Lang, G. Candler, P. Dimotakis, Simulating schlieren and shadowgraph images from LES data, Experiments in Flu-

ids 60 (2019) 1–16. URL: https://doi.org/10.1007/s00348-019-2774-6https://link.springer.com/content/pdf/10.1007/s00348-019-2774-6.pdf. doi:10.1007/s00348-019-2774-6.

[74] H. Schlichting, K. Gersten, Boundary-Layer Theory, 2016.

[75] N. Standen, Calculation of integral parameters of a compressible turbulent boundary layer using a concept of mass entrainment, Ph.D. thesis, 1964. URL: https://central.bac-lac.gc.ca/.item?id=TC-QMM-116688&op=pdf&app=Library&oclc_number=894354999.

[76] J. P. Hickey, K. Younes, M. X. Yao, D. Fan, J. Mouallem, Targeted turbulent structure control in wall-bounded flows via localized heating, Physics of Fluids 32 (2020). URL: https://doi.org/10.1063/1.5144387. doi:10.1063/1.5144387.

[77] S. N. A. Yusof, Y. Asako, N. A. C. Sidik, S. B. Mohamed, W. M. A. A. Japar, A short review on rans turbulence models, 2020. doi:10.37934/cfdl.12.11.8396.

[78] C. L. Liu, H. R. Zhu, J. T. Bai, Effect of turbulent Prandtl number on the computation of film-cooling effectiveness, International Journal of Heat and Mass Transfer 51 (2008) 6208–6218. URL: http://dx.doi.org/10.1016/j.ijheatmasstransfer.2008.04.039. doi:10.1016/j.ijheatmasstransfer.2008.04.039.

[79] S. Roy, U. Pathak, K. Sinha, Variable turbulent prandtl number model for shock/boundary-layer interaction, AIAA Journal 56 (2018) 342–355. doi:10.2514/1.J056183.

[80] S. Roy, K. Sinha, F. Lacombe, J. P. Hickey, Anisotropic turbulent heat flux modelling through shock waves, in: AIAA Aviation 2019 Forum, 2019, pp. 1–11. doi:10.2514/6.2019-3321.

[81] F. Lacombe, S. Roy, K. Sinha, S. Karl, J.-P. Hickey, Characteristic scales in shock–turbulence interaction, AIAA Journal 59 (2021) 526–532. URL: https://doi.org/10.2514/1.J059499. doi:10.2514/1.J059499. arXiv:https://doi.org/10.2514/1.J059499.

[82] G. Masuya, N. Chinzei, S. Ishii, Secondary gas injection into a supersonic conical nozzle, AIAA Journal 15 (1977) 301–302. doi:10.2514/3.63234.

[83] M. Sellam, A. Chpoun, V. Zmijanovic, V. Lago, Fluidic thrust vectoring of an axisymmetrical nozzle: an analytical model, International Journal of Aerodynamics 2 (2012) 193. doi:10.1504/ijad.2012.049112.